An anisotropic permeability model for coal considering stress sensitivity, matrix anisotropic internal swelling/shrinkage, and gas rarefaction effects

Journal:	*Energy & Fuels*
Manuscript ID	ef-2022-04003r.R2
Manuscript Type:	Article
Date Submitted by the Author:	24-Jan-2023

Complete List of Authors:	Zeng, Jie; Southwest Petroleum University Guo, Jianchun; Southwest Petroleum University, 2. School of Petroleum Engineering Liu, Jishan ; University of Western Australia, Li, Wai; The University of Western Australia Zhou, Yingfang; University of Aberdeen, School of Engineering Tian, Jianwei; Technical University of Denmark

An anisotropic permeability model for coal considering stress sensitivity, matrix anisotropic internal swelling/shrinkage, and gas rarefaction effects

Jie Zeng[a]*, Jianchun Guo[a]*, Jishan Liu[b], Wai Li[b], Yingfang Zhou[c], Jianwei Tian[d]

[a] State Key Laboratory of Oil and Gas Reservoir Geology and Exploitation, Southwest Petroleum University, Chengdu Sichuan, 610500, China

[b] Department of Chemical Engineering, School of Engineering, The University of Western Australia, 35 Stirling Highway, WA, 6009, Australia

[c] School of Engineering, University of Aberdeen, AB24 3UE, Aberdeen, UK

[d] Danish Offshore Technology Centre, Technical University of Denmark, 2800 Lyngby, Denmark

Corresponding author E-mail address: jie.zeng@swpu.edu.cn (J. Zeng), guojianchun@vip.163.com (J. Guo)

Abstract

Permeability is the most crucial property of coal in relation to coalbed methane (CBM) production and CO_2 sequestration. Due to coal's anisotropic structure and mechanical properties, its permeability exhibits strong anisotropy. The main factors controlling coal permeability evolution are effective stress, anisotropic swelling/shrinkage near fracture surfaces (internal swelling/shrinkage), and gas rarefaction effects. Combined impacts of the above mechanisms make coal permeability evolution complex and difficult to predict. In this study, we establish a full anisotropic coal permeability model incorporating stress sensitivity, anisotropic internal swelling/shrinkage, and gas rarefaction effects. Specifically, a mechanical-property-based internal swelling model is established to link up anisotropic internal swelling/shrinkage with mechanical anisotropy, using the energy balance theory. A Knudsen-number-based model is utilized to describe gas rarefactions effects. The comparison with coal anisotropic swelling data and anisotropic permeability evolution data demonstrates permeability model's reliability. Results show that anisotropic internal swelling/shrinkage mainly determines the overall shape of permeability curves, the evolution trend, the range of permeability change in all directions, and the anisotropy level during evolution. It partially or totally offsets the permeability change caused by effective stress variation under certain stress conditions. Effective stress variation starts to dominate permeability evolution when the variation exceeds a certain value. Permeability increment/reduction caused by gas rarefaction phenomenon enhancement/weakening is dependent on fracture (pore) pressure and aperture but its influence on permeability is not as strong as that of anisotropic internal swelling/shrinkage. Anisotropic internal swelling/shrinkage and the gas rarefaction phenomenon show a synergistic influence on anisotropic permeability evolution with fracture (pore) pressure changing. The permeability model is applicable for different permeability measurement conditions.

1. Introduction

The performance of CBM production and long-term CO_2 geological sequestration in coalbeds is heavily dependent on coal permeability [1,2]. Coal is generally anisotropic and consists of three sets of main flow channels, videlicet, face cleats, butt cleats, and bedding planes [3]. Therefore, coal permeability shows strong anisotropy [4]. Unlike conventional gas reservoirs, the large internal surface area provides sufficient place for gas adsorption [5]. Gas adsorption/desorption causes a surface energy change which leads to coal matrix and bulk rock swelling/shrinkage [6]. The magnitudes of swelling/shrinkage in different directions can be substantially different (anisotropic swelling/shrinkage) [6–8]. When gas flows through coal, gas pressure variation (effective stress variation) changes the fracture (cleat) aperture, resulting in permeability evolution [9,10]. Meanwhile, gas adsorption/desorption induces swelling/shrinkage of coal matrices near the fracture (cleat) surface (internal surface), which narrows/opens the fractures (cleats) and reduces/ increases coal permeability [9–11]. This swelling/shrinkage phenomenon is called internal swelling/shrinkage and is regarded as a key factor affecting coal permeability evolution [6,9]. In addition, the impact of the gas rarefaction phenomenon (gas slippage) on permeability has been widely observed in different experiments [12–16]. For the small flow channels within coal, the permeability is also influenced by gas rarefaction effects [13,14,17,18], which lead to invalid classical permeability effective stress laws [19]. Due to the aforementioned factors, it is challenging to accurately describe anisotropic coal permeability evolution in the process of gas injection/extraction under the combined effects of effective stress, anisotropic internal swelling/shrinkage, and the gas rarefaction phenomenon.

In the literature, a variety of coal permeability models have been established. These models involve key parameters that describe coal properties, including Young's modulus, Poisson's ratio, adsorption and swelling strain constants, and compressibility [20]. However, the majority of coal permeability models did not incorporate the anisotropic nature of coal. As for anisotropic coal permeability models, Table 1 summarizes some typical ones and the permeability evolution mechanisms they considered. Wu et al. [21] developed directional permeability-strain relations and found that coal permeability is dominated by boundary conditions, fracture distributions, and matrix-fracture interactions. That coal cleat permeability model considers anisotropic effective strains with the impact of matrix swelling/shrinkage, but ignores anisotropic swelling and gas rarefaction effects. To understand the link between coal permeability variation and directional strains, Liu et al. [22] used a modulus reduction ratio which is the ratio of the coal bulk elastic modulus to coal matrix modulus. In that permeability model, the effective strains are anisotropic, but the swelling strains in different directions are identical (1/3 of the volumetric swelling strain). Pan and Connell [6] added anisotropic swelling into the Shi and Durucan permeability relationship [5] and proposed direction permeability models. Their work incorporates anisotropic swelling and structural anisotropy. Nevertheless, the permeability model is derived under simplified conditions and requires further improvement when coal mechanical properties and swelling in the two horizontal directions are not identical. Wang et al. [8] incorporated directional compaction, directional swelling, and high-velocity non-Darcy flow to investigate gas extraction in coal seams. In their model, the Langmuir equation is extended to depict anisotropic swelling strains. However, they simply used three sets of independent Langmuir pressure and swelling strain constants to quantify anisotropic swelling without including matrix's anisotropic mechanical properties. This may not be theoretically appropriate, and the model can be treated as an empirical one. Then, Wang et al. [23] derived an anisotropic coal permeability model with consideration of anisotropic mechanical properties and gas-sorption-induced anisotropic internal swelling. That model incorporates matrix anisotropic swelling's contribution to fracture (cleat) aperture modification (anisotropic internal swelling) and is suitable for different boundary conditions. However, they still used three sets of independent Langmuir pressure and swelling strain constants to describe anisotropic swelling and ignored possible gas rarefaction effects. Later, Moore et al. [24] formalized a transversely isotropic coal permeability model for vertically cleated coal rocks. Five elastic stiffness parameters (two Young's moduli and three Poisson's ratios) were used in their model. That model ignores anisotropic swelling and gas rarefaction effects. In the same year, An et al. [2] presented an anisotropic permeability model that employs adsorbed-gas mass and anisotropic Young's moduli to calculate anisotropic swelling strains. The way they simulate directional swelling is more reasonable compared with those merely using three sets of independent Langmuir parameters, but internal swelling and gas rarefaction effects are still not included. Then, Zhang et al. [25] established an anisotropic permeability model that couples stress evolution, gas adsorption/desorption, and microfracture propagation. They did not link up anisotropy swelling behavior with anisotropic mechanical properties. To investigate the role of anisotropy in permeability evolution, Wang et al. [10] derived analytical pressure-permeability expressions based on a coal representative element under oedometric and isochoric conditions. That model uses isotropic adsorption stress and anisotropic stiffness coefficients to simulate anisotropic swelling but is only applicable for specific conditions. Gas rarefaction effects are also neglected. More recently, Li et al. [26] proposed an anisotropic coal permeability model considering combined effects of effective stress variation and gas slippage. As for gas slippage, they used a slip factor similar to Klinkenberg's model [27]. However, the slip-factor correction for gas slippage is not as accurate as the Beskok-Karniadakis model [28] suitable for the full-range gas rarefied flow.

Table 1 Typical anisotropic coal permeability models and their features

Models	Model description	Factors affecting permeability evolution
Wu et al. (2010) [21]	An anisotropic cleat permeability model involving stress sensitivity and matrix swelling/shrinkage	Stress sensitivity and matrix swelling/shrinkage
Liu et al. (2010) [22]	An anisotropic model linking the permeability change to directional strains through an elastic modulus reduction ratio	Stress sensitivity and anisotropic effective strains (isotropic swelling strains)
Pan and Connell (2011) [6]	An anisotropic permeability expression considering anisotropic swelling under simplified conditions	Stress sensitivity and anisotropic swelling (under simplified conditions)
Wang et al. (2013) [8]	An anisotropic permeability model involving non-Darcy flow and anisotropic swelling depicted by three sets of Langmuir pressure and swelling strain constants	Stress sensitivity, non-Darcy flow, and anisotropic swelling (described by three sets of independent Langmuir parameters)
Wang et al. (2014) [23]	A general anisotropic permeability model involving anisotropic internal swelling depicted by three sets of Langmuir pressure and swelling strain constants	Stress sensitivity, anisotropic internal swelling (described by three sets of independent Langmuir parameters), and different boundary conditions
Moore et al. (2015) [24]	A transversely isotropic coal permeability model	Stress sensitivity and matrix swelling (under transversely isotropic conditions)
An et al. (2015) [2]	An anisotropic permeability model using adsorbed-gas mass and anisotropic Young's moduli to calculate anisotropic swelling strains	Stress sensitivity and anisotropic swelling (described by adsorbed-gas mass and anisotropic Young's moduli)
Zhang et al. (2017) [25]	An anisotropic permeability model considering microfracture-propagation-induced strain variation and anisotropic internal swelling	Stress sensitivity, microfracture-propagation-induced strain variation, and sorption-induced anisotropic internal swelling (described by three sets of independent Langmuir parameters)
Wang et al. (2018)	An anisotropic permeability model using an isotropic adsorption stress and	Stress sensitivity and anisotropic swelling under

[10]	anisotropic stiffness coefficients to simulate anisotropic swelling under specific conditions	oedometric and isochoric conditions
Li et al. (2021) [26]	An anisotropic permeability model involving combined effects of effective stress variation and gas slippage	Stress sensitivity and gas slippage

From the above literature review, one can find that these models may be versatile enough for characterizing anisotropic coal permeability evolution under certain conditions. However, most existing models ignored gas rarefaction effects and anisotropic internal swelling/shrinkage or did not appropriately describe anisotropic internal swelling/shrinkage. In this research, we propose a generic anisotropic coal permeability model with a particular emphasis on accurately and appropriately describing anisotropic internal swelling/shrinkage and gas rarefaction effects. A new mechanical-property-based anisotropic internal swelling model is established to link anisotropic internal swelling/shrinkage behavior with mechanical anisotropy based on the energy balance theory and a modified sugar-cube conceptual coal model. The gas rarefaction phenomenon is depicted by a Knudsen-number-based model. The anisotropic swelling model is validated by comparing with coal anisotropic swelling data. The proposed permeability model is verified against anisotropic permeability evolution data collected under constant fracture (cleat) pressure and constant confining pressure conditions. It is also suitable for constant effective stress conditions. Finally, the verified permeability model is applied to analyze the roles of matrix directional internal swelling/shrinkage and gas rarefaction effects on permeability evolution.

2. Model development

To derive the anisotropic swelling and permeability models, we apply a structure model modified from the classical sugar-cube model [29]. In this section, the conceptual structure used for model derivation and the assumptions we made are introduced first. Then, detailed derivation of anisotropic internal swelling and permeability models is presented.

2.1 Conceptual model

Coal contains two sets of vertical cleats (face and butt cleats) and one set of bedding planes. Such a material can be idealized as a modified sugar-cube conceptual model, as shown in Fig. 1. Matrix blocks are separated by these fractures (cleats or bedding planes) so that parts of sorption/desorption-induced matrix block swelling/shrinkage purely contribute to fracture (cleat) aperture variation [30,31]. This effect is called internal swelling/shrinkage (see Fig. 2). The fracture aperture is b (m), while the spacing is a (m). Because fracture (cleat) permeability is far larger than coal matrix permeability, we follow most researchers' work and attribute coal permeability to fracture (cleat) permeability [31]. Other assumptions we made are as follows: (1) Coal is saturated by methane or CO_2 under an isothermal condition. The aperture of face cleats, butt cleats, and bedding planes is not identical, while the matrix block side-length can be either identical or different. (2) The mechanical properties of coal are anisotropic. (3) The total volumetric swelling strain is proportional to the amount of adsorbed gas and is described through the Langmuir-type equation[32]. The anisotropic swelling/shrinkage process occurs instantaneously with the change of pore (fracture) pressure [8]. Note that the fracture (cleat) aperture, spacing, and matrix block size are equivalent ones for permeability modeling. Thus, they could be different from the directly measured aperture and matrix block size. These flow channels can also represent micro-cleats with very small aperture.

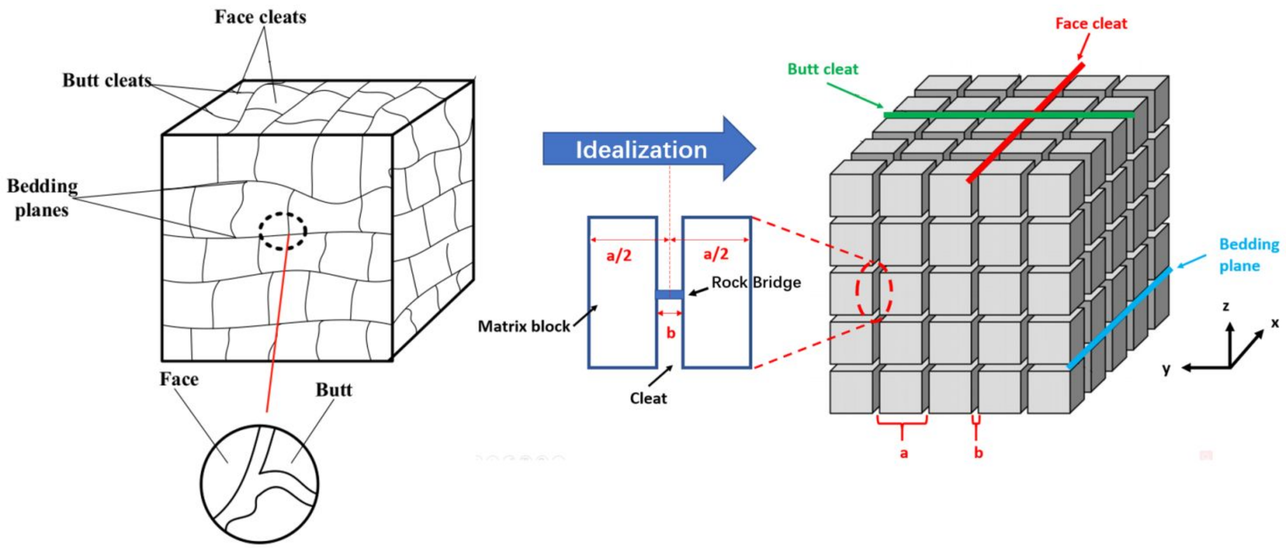

Fig. 1 Schematic of the fracture system (cleats and bedding planes) and matrix blocks (modified from Li et al. [33] and Wang et al. [23] with permission from [33] Elsevier. Copyright 2022 and [23] Elsevier. Copyright 2014).

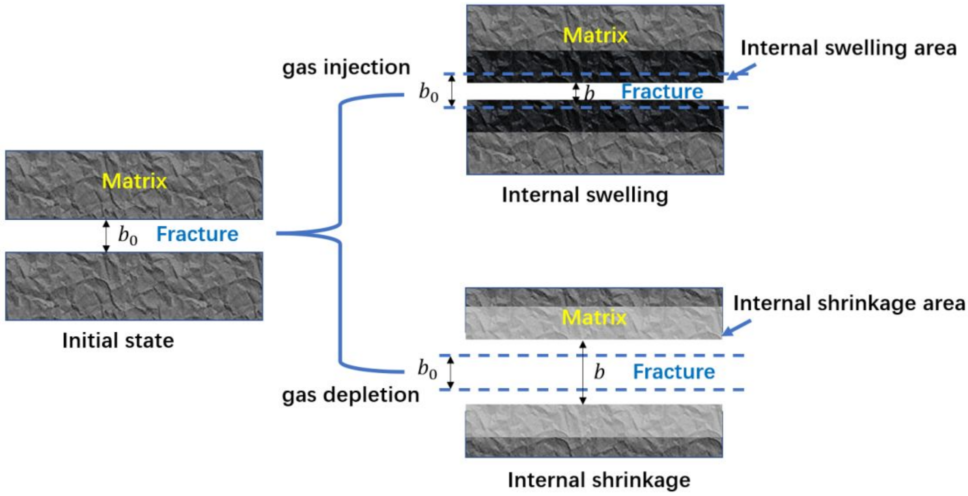

Fig. 2 Schematic of internal swelling/shrinkage near the fracture (cleat) surface (the black area is the internal swelling area, while the light gray area is the internal shrinkage area).

2.2 Formulation of the permeability model

Based on the conceptual model of Fig. 1, the flow channel spacing and aperture are defined as a_{face}, b_{face}, a_{butt}, b_{butt}, a_{bed}, and b_{bed} respectively, where the subscripts represent the corresponding flow channel type. Accordingly, the porosity contributed by each fracture (cleat) system is written as [23,25]

$$\phi_{face} = \frac{b_{face}}{a_{face}}, \tag{1}$$

$$\phi_{butt} = \frac{b_{butt}}{a_{butt}}, \tag{2}$$

$$\phi_{bed} = \frac{b_{bed}}{a_{bed}}. \tag{3}$$

The total porosity contributed by the three fracture (cleat) systems is

$$\phi = \phi_{face} + \phi_{butt} + \phi_{bed}. \tag{4}$$

The intrinsic permeability of each fracture (cleat) system can be written as [29,34]

$$k_{face} = \frac{b_{face}^2}{12}, \tag{5}$$

$$k_{butt} = \frac{b_{butt}^2}{12}, \tag{6}$$

$$k_{bed} = \frac{b_{bed}^2}{12}. \tag{7}$$

Then, the corresponding bulk permeability can be expressed as [29,34]

$$k_{face,b} = \frac{b_{face}^2 \Phi_{face}}{12} = \frac{b_{face}^3}{12a_{face}}, \tag{8}$$

$$k_{butt,b} = \frac{b_{butt}^2 \Phi_{butt}}{12} = \frac{b_{butt}^3}{12a_{butt}}, \tag{9}$$

$$k_{bed,b} = \frac{b_{bed}^2 \Phi_{bed}}{12} = \frac{b_{bed}^3}{12a_{bed}}. \tag{10}$$

Here, a comma followed by subscript *b* denotes bulk properties. Considering gas rarefaction effects, the apparent permeability concept is applied here. According to Beskok and Karniadakis [28], the permeability terms in Eqs. 8 to 10 are modified into apparent permeability terms

$$k_{face,bapp} = \frac{b_{face}^3}{12a_{face}} C(\xi_{face})(1 + \omega_{face} Kn_{face})\left(1 + \frac{6Kn_{face}}{1 + Kn_{face}}\right), \tag{11}$$

$$k_{butt,bapp} = \frac{b_{butt}^3}{12a_{butt}} C(\xi_{butt})(1 + \omega_{butt} Kn_{butt})\left(1 + \frac{6Kn_{butt}}{1 + Kn_{butt}}\right), \tag{12}$$

$$k_{bed,bapp} = \frac{b_{bed}^3}{12a_{bed}} C(\xi_{bed})(1 + \omega_{bed} Kn_{bed})\left(1 + \frac{6Kn_{bed}}{1 + Kn_{bed}}\right), \tag{13}$$

where $C(\xi)$ is the correction factor for a certain cross-sectional area; ξ is the aspect ratio defined as a/b; Kn is the Knudsen number defined as the ratio of the molecular mean free path (l_{mean}) to the flow channel aperture (b) [28]. Here, the mean free path can be calculated as follow [35,36]: $l_{mean} = K_B T / (\sqrt{2}\pi d_m^2 p)$, where K_B is the Boltzmann constant (1.3806×10^{-23} J/K); T is the temperature (K); d_m is the gas molecule diameter (m); and p is the pore (cleat) pressure (MPa). ω is a coefficient of the Beskok-Karniadakis model [28]:

$$\omega = \frac{128}{15\pi^2} \tan^{-1}(4Kn^{0.4}). \tag{14}$$

The first terms in the right side of Eqs. 11 to 13 are the above-mentioned bulk permeability. By adding the gas rarefaction effect and flow channel shape correction term: $C(\xi)(1+\omega Kn)$ $\left[1+{}^{6Kn}/_{(1+Kn)}\right]$ [28], they can describe apparent permeability. Because $a \gg b$, $C(\xi) \approx 1$. Thus, the apparent permeability terms are simplified as

$$k_{face,bapp} = \frac{b_{face}^3}{12a_{face}}\left(1+\omega_{face}Kn_{face}\right)\left(1+\frac{6Kn_{face}}{1+Kn_{face}}\right), \tag{15}$$

$$k_{butt,bapp} = \frac{b_{butt}^3}{12a_{butt}}\left(1+\omega_{butt}Kn_{butt}\right)\left(1+\frac{6Kn_{butt}}{1+Kn_{butt}}\right), \tag{16}$$

$$k_{bed,bapp} = \frac{b_{bed}^3}{12a_{bed}}\left(1+\omega_{bed}Kn_{bed}\right)\left(1+\frac{6Kn_{bed}}{1+Kn_{bed}}\right). \tag{17}$$

The flow channel spacing ratio is very close to one (${}^{a}/_{a_0} \approx 1$), and its impact on permeability evolution is negligible compared with that of the porosity ratio [37]. Thus, based on Eqs. 1 to 3 and Eqs. 15 to 17, the following apparent permeability expressions are obtained

$$k_{face,bapp} = k_{face,bapp0}\left(\frac{\phi_{face}}{\phi_{face0}}\right)^3\left(\frac{a_{face}}{a_{face0}}\right)^2\frac{\left(1+\omega_{face}Kn_{face}\right)\left(1+\frac{6Kn_{face}}{1+Kn_{face}}\right)}{\left(1+\omega_{face0}Kn_{face0}\right)\left(1+\frac{6Kn_{face0}}{1+Kn_{face0}}\right)} \approx k_{face,bapp0}\left(\frac{\phi_{face}}{\phi_{face0}}\right)^3 \frac{\left(1+\omega_{face}Kn_{face}\right)\left(1+\frac{6Kn_{face}}{1+Kn_{face}}\right)}{\left(1+\omega_{face0}Kn_{face0}\right)\left(1+\frac{6Kn_{face0}}{1+Kn_{face0}}\right)}, \tag{18}$$

$$k_{butt,bapp} = k_{butt,bapp0}\left(\frac{\phi_{butt}}{\phi_{butt0}}\right)^3\left(\frac{a_{butt}}{a_{butt0}}\right)^2\frac{\left(1+\omega_{butt}Kn_{butt}\right)\left(1+\frac{6Kn_{butt}}{1+Kn_{butt}}\right)}{\left(1+\omega_{butt0}Kn_{butt0}\right)\left(1+\frac{6Kn_{butt0}}{1+Kn_{butt0}}\right)} \approx k_{butt,bapp0}\left(\frac{\phi_{butt}}{\phi_{butt0}}\right)^3 \frac{\left(1+\omega_{butt}Kn_{butt}\right)\left(1+\frac{6Kn_{butt}}{1+Kn_{butt}}\right)}{\left(1+\omega_{butt0}Kn_{butt0}\right)\left(1+\frac{6Kn_{butt0}}{1+Kn_{butt0}}\right)}, \tag{19}$$

$$k_{bed,bapp} = k_{bed,bapp0}\left(\frac{\phi_{bed}}{\phi_{bed0}}\right)^3\left(\frac{a_{bed}}{a_{bed0}}\right)^2\frac{\left(1+\omega_{bed}Kn_{bed}\right)\left(1+\frac{6Kn_{bed}}{1+Kn_{bed}}\right)}{\left(1+\omega_{bed0}Kn_{bed0}\right)\left(1+\frac{6Kn_{bed0}}{1+Kn_{bed0}}\right)} \approx k_{bed,bapp0}\left(\frac{\phi_{bed}}{\phi_{bed0}}\right)^3 \frac{\left(1+\omega_{bed}Kn_{bed}\right)\left(1+\frac{6Kn_{bed}}{1+Kn_{bed}}\right)}{\left(1+\omega_{bed0}Kn_{bed0}\right)\left(1+\frac{6Kn_{bed0}}{1+Kn_{bed0}}\right)}. \tag{20}$$

As illustrated in Fig. 1, in each direction, there are two sets of fracture (cleat) systems that serve as gas flow channels parallelly. Therefore, the directional permeability can be expressed as

$$k_x = c_x\left(k_{face,bapp} + k_{bed,bapp}\right), \tag{21}$$

$$k_y = c_y(k_{butt,bapp} + k_{bed,bapp}), \tag{22}$$

$$k_z = c_z(k_{butt,bapp} + k_{face,bapp}). \tag{23}$$

Here, c_x, c_y, and c_z are the connectivity-tortuosity correction coefficients (0~1). For some simple cases, this correction coefficient is 1, which means the conceptual geometry can directly and equivalently represent coal without further considering connectivity or tortuosity. Because the initial directional permeability values and tortuosity data are known, one can obtain the following group of equations

$$\begin{cases} k_{x0} = c_x(k_{face,bapp0} + k_{bed,bapp0}) \\ k_{y0} = c_y(k_{butt,bapp0} + k_{bed,bapp0}) \\ k_{z0} = c_z(k_{butt,bapp0} + k_{face,bapp0}) \end{cases}. \tag{24}$$

The above equation group can be solved and provides the permeability of each fracture (cleat) system

$$k_{butt,bapp0} = \frac{{}^{k_{y0}}/_{c_y} + {}^{k_{z0}}/_{c_z} - {}^{k_{x0}}/_{c_x}}{2}, \tag{25}$$

$$k_{face,bapp0} = \frac{{}^{k_{x0}}/_{c_x} + {}^{k_{z0}}/_{c_z} - {}^{k_{y0}}/_{c_y}}{2}, \tag{26}$$

$$k_{bed,bapp0} = \frac{{}^{k_{x0}}/_{c_x} + {}^{k_{y0}}/_{c_y} - {}^{k_{z0}}/_{c_z}}{2}. \tag{27}$$

At this stage, the only unknows for permeability calculation are the porosity ratios and the dynamic fracture (cleat) aperture. Here, the initial aperture and spacing can be obtained by matching with initial apparent permeability [38]. The porosity ratios and fracture (cleat) aperture variation can be calculated via the poroelasticity theory. Take the face cleat as an example, the porosity increment is given by [23,32,39]

$$\mathrm{d}\phi_{face} = \mathrm{d}\left(\frac{b_{face}}{a_{face}}\right) = \frac{a_{face}\mathrm{d}b_{face} - b_{face}\mathrm{d}a_{face}}{(a_{face})^2} = \phi_{face}\left(\frac{\mathrm{d}b_{face}}{b_{face}} - \frac{\mathrm{d}a_{face}}{a_{face}}\right), \tag{28}$$

Extending the poroelasticity theory for isotropic porous media to that for anisotropic porous media yields [32]

$$\frac{\mathrm{d}a_{face}}{a_{face}} = -\,\mathrm{d}\varepsilon_{y,b} = -\frac{\mathrm{d}\sigma_{ey}}{E_{y,b}} + \frac{\nu_{xy,b}\mathrm{d}\sigma_{ex}}{E_{x,b}} + \frac{\nu_{zy,b}\mathrm{d}\sigma_{ez}}{E_{z,b}} + \mathrm{d}\varepsilon_{bsy}, \tag{29}$$

$$\frac{\mathrm{d}b_{face}}{b_{face}} = -\,\mathrm{d}\varepsilon_{y,c} = -\frac{\mathrm{d}\sigma_{ey}}{E_{y,c}} + \frac{\eta_{xy,c}\mathrm{d}\sigma_{ex}}{E_{x,c}} + \frac{\eta_{zy,c}\mathrm{d}\sigma_{ez}}{E_{z,c}} + \mathrm{d}\varepsilon_{bsy} + \mathrm{d}\varepsilon_{fsy}, \tag{30}$$

where $\sigma_{ei} = \sigma_i - \alpha_i p$ ($i = x$, y, or z), and the Biot coefficient α_i is normally assumed to be equal to unity for anisotropic models [23]. Here, E is the Young's modulus (Pa) and ν is the Poisson's ratio. In Eqs. 29 and 30, subscript b represents bulk properties; subscript c denotes the fracture (cleat) system properties; ε_{bsi} is the bulk linear swelling strain in the i direction which simultaneously increases fracture (cleat) aperture and spacing with the same proportion [32]; and ε_{fsi} is the corresponding linear swelling strain of fracture systems. Note that $\eta_{xy,c}$ and $\eta_{zy,c}$ in Eq. 30 are two parameters similar to Poisson's ratio, but their values can be very small because of matrix-fracture (cleat) interaction. Under some limiting conditions, matrix block's compaction may narrow adjacent flow channels. For example, when the vertical effective stress increases, the lateral expansion of matrix blocks may narrow the two sets of vertical cleats. Similar to Liu et al. [40], the bulk and fracture (cleat) moduli satisfy $E_b/E_c = R_c$, where R_c is a constant. Consequently, Eq. 28 can be written as

$$\mathrm{d}\phi_{face} = \phi_{face}\left(-\frac{\mathrm{d}\sigma_{ey}}{E_{y,c}} + \frac{\eta_{xy,c}\mathrm{d}\sigma_{ex}}{E_{x,c}} + \frac{\eta_{zy,c}\mathrm{d}\sigma_{ez}}{E_{z,c}} + \mathrm{d}\varepsilon_{fsy} + \frac{\mathrm{d}\sigma_{ey}}{E_{y,b}} - \frac{\nu_{xy,b}\mathrm{d}\sigma_{ex}}{E_{x,b}} - \frac{\nu_{zy,b}\mathrm{d}\sigma_{ez}}{E_{z,b}}\right) = \phi_{face}$$
$$\left[(1-R_c)\frac{\mathrm{d}\sigma_{ey}}{E_{y,b}} - (\nu_{xy,b} - \eta_{xy,c}R_c)\frac{\mathrm{d}\sigma_{ex}}{E_{x,b}} - (\nu_{zy,b} - \eta_{zy,c}R_c)\frac{\mathrm{d}\sigma_{ez}}{E_{z,b}} + \mathrm{d}\varepsilon_{fsy}\right], \tag{31}$$

where ε_{fsy} is the directional linear swelling strain within fractures (cleats) in the y direction and can be converted from the directional matrix linear swelling strain (ε_{msy}). Anisotropic swelling of coal has been experimentally observed with the injection of adsorbate, such as CO_2 and methane [6,7,41]. To match with experimental data, some researchers used three sets of Langmuir pressure and swelling strain constants in three Langmuir equations to describe the linear swelling strains in the three principal directions [8,23,25]. These directional swelling equations are much simpler than those of Pan and Connell [6]. However, it may not be theoretically appropriate to use three sets of independent Langmuir coefficients for a single material without considering its anisotropic mechanical properties. Besides, the Langmuir equation is basically an empirical one for calculating volumetric strains under stress-controlled conditions. Of course, one can use the Langmuir equation to calculated the total volumetric strain and divide it into three components to represent the linear strains in three directions, but the weighting factor for each component is unknown. In this paper, based on the anisotropic mechanical properties of coal, a new anisotropic swelling model is derived to calculate directional linear swelling strains. Then, by using the internal swelling factor [30,31], the anisotropic swelling model is converted into an anisotropic internal swelling model. Next, detailed derivation of the anisotropic internal swelling model is shown. Because shrinkage is an inverse process of swelling, this model is also applicable for anisotropic internal shrinkage. The Langmuir equation is used to describe the overall sorption-induced matrix volumetric strain[32,42]

$$\varepsilon_{msV} = \varepsilon_{ms}\frac{p}{p + p_{mL}}, \tag{32}$$

where ε_{ms} is the matrix Langmuir strain constant, and p_{mL} is the matrix Langmuir pressure (Pa). Considering that the deformation is viewed along the three principal directions and the swelling strains are small, the overall sorption-induced volumetric strain can be expressed as the sum of sorption-induced linear strains [7]

$$\varepsilon_{msV} = \varepsilon_{msx} + \varepsilon_{msy} + \varepsilon_{msz}, \tag{33}$$

where ε_{msx}, ε_{msy}, and ε_{msz} are sorption-induced linear swelling strains in the three directions. For a porous medium, when surface energy changes by adsorption of gas or other adsorbate, there is a consequent dilatation of the body [43]. Thus, there is a strain caused by surface-energy-change-induced deformation. The elastic energy change is equal to the surface energy change [6,43]. As demonstrated in Fig. 1, the void space that separates matrix blocks are cleats or bedding planes. Thus, when matrices swell, matrix blocks deform freely towards the void space (fractures or cleats) without any external displacement constrains [44]. Matrix block swelling can be treated as free swelling. The equivalent mean normal stress caused by swelling under a free swelling condition is $\overline{\sigma_s}$. Then, matrix sorption-induced linear strains in the three directions are

$$\varepsilon_{msx} = \frac{\overline{\sigma_s}}{E_{x,m}} - \frac{\nu_{yx,m}\overline{\sigma_s}}{E_{y,m}} - \frac{\nu_{zx,m}\overline{\sigma_s}}{E_{z,m}}, \tag{34}$$

$$\varepsilon_{msy} = \frac{\overline{\sigma_s}}{E_{y,m}} - \frac{\nu_{xy,m}\overline{\sigma_s}}{E_{x,m}} - \frac{\nu_{zy,m}\overline{\sigma_s}}{E_{z,m}}, \tag{35}$$

$$\varepsilon_{msz} = \frac{\overline{\sigma_s}}{E_{z,m}} - \frac{\nu_{xz,m}\overline{\sigma_s}}{E_{x,m}} - \frac{\nu_{yz,m}\overline{\sigma_s}}{E_{y,m}}, \tag{36}$$

where the subscript *m* represents matrix properties. Combining Eqs. 32 to 36 yields

$$\varepsilon_s\frac{p}{p+p_{mL}} = \overline{\sigma_s}\left(\frac{1}{E_{x,m}} - \frac{\nu_{yx,m}}{E_{y,m}} - \frac{\nu_{zx,m}}{E_{z,m}} + \frac{1}{E_{y,m}} - \frac{\nu_{xy,m}}{E_{x,m}} - \frac{\nu_{zy,m}}{E_{z,m}} + \frac{1}{E_{z,m}} - \frac{\nu_{xz,m}}{E_{x,m}} - \frac{\nu_{yz,m}}{E_{y,m}}\right). \tag{37}$$

Note that Poisson's ratios and Young's moduli in the above equation satisfy the following relationship [20]: $\frac{\nu_{yx,m}}{E_{y,m}} = \frac{\nu_{xy,m}}{E_{x,m}}$, $\frac{\nu_{zx,m}}{E_{z,m}} = \frac{\nu_{xz,m}}{E_{x,m}}$, and $\frac{\nu_{zy,m}}{E_{z,m}} = \frac{\nu_{yz,m}}{E_{y,m}}$. Thus, Eq. 37 becomes

$$\varepsilon_s\frac{p}{p+p_{mL}} = \overline{\sigma_s}\left(\frac{1}{E_{x,m}} + \frac{1}{E_{y,m}} + \frac{1}{E_{z,m}} - \frac{2\nu_{yx,m}}{E_{y,m}} - \frac{2\nu_{xz,m}}{E_{x,m}} - \frac{2\nu_{zy,m}}{E_{z,m}}\right). \tag{38}$$

Since the directional moduli of matrices and the bulk rock approximately satisfy $\frac{E_{x,m}}{E_{x,b}} = \frac{E_{y,m}}{E_{y,b}} = \frac{E_{z,m}}{E_{z,b}}$ [45], and bulk rock Poisson's ratios are approximated equal to those of matrix blocks, the linear swelling strains in the three directions are

$$\varepsilon_{m\,sx} = \varepsilon_s\frac{p}{p+p_{mL}}\frac{\left(\frac{1}{E_{x,m}} - \frac{\nu_{yx,m}}{E_{y,m}} - \frac{\nu_{zx,m}}{E_{z,m}}\right)}{\left(\frac{1}{E_{x,m}} - \frac{\nu_{yx,m}}{E_{y,m}} - \frac{\nu_{zx,m}}{E_{z,m}} + \frac{1}{E_{y,m}} - \frac{\nu_{xy,m}}{E_{x,m}} - \frac{\nu_{zy,m}}{E_{z,m}} + \frac{1}{E_{z,m}} - \frac{\nu_{xz,m}}{E_{x,m}} - \frac{\nu_{yz,m}}{E_{y,m}}\right)} = \varepsilon_s\frac{p}{p+p_{mL}}\frac{\left(\frac{1}{E_{x,m}} - \frac{\nu_{yx,m}}{E_{y,m}} - \frac{\nu_{xz,m}}{E_{x,m}}\right)}{\left(\frac{1}{E_{x,m}} + \frac{1}{E_{y,m}} + \frac{1}{E_{z,m}} - \frac{2\nu_{yx,m}}{E_{y,m}} - \frac{2\nu_{xz,m}}{E_{x,m}} - \frac{2\nu_{zy,m}}{E_{z,m}}\right)} = \varepsilon_s\frac{p}{p+p_{mL}}\frac{\left(\frac{1}{E_{x,b}} - \frac{\nu_{yx,b}}{E_{y,b}} - \frac{\nu_{xz,b}}{E_{x,b}}\right)}{\left(\frac{1}{E_{x,b}} + \frac{1}{E_{y,b}} + \frac{1}{E_{z,b}} - \frac{2\nu_{yx,b}}{E_{y,b}} - \frac{2\nu_{xz,b}}{E_{x,b}} - \frac{2\nu_{zy,b}}{E_{z,b}}\right)}, \tag{39}$$

$$\varepsilon_{msy} = \varepsilon_s\frac{p}{p+p_{mL}}\frac{\left(\frac{1}{E_{y,m}} - \frac{\nu_{xy,m}}{E_{x,m}} - \frac{\nu_{zy,m}}{E_{z,m}}\right)}{\left(\frac{1}{E_{x,m}} - \frac{\nu_{yx,m}}{E_{y,m}} - \frac{\nu_{zx,m}}{E_{z,m}} + \frac{1}{E_{y,m}} - \frac{\nu_{xy,m}}{E_{x,m}} - \frac{\nu_{zy,m}}{E_{z,m}} + \frac{1}{E_{z,m}} - \frac{\nu_{xz,m}}{E_{x,m}} - \frac{\nu_{yz,m}}{E_{y,m}}\right)} = \varepsilon_s\frac{p}{p+p_{mL}}\frac{\left(\frac{1}{E_{y,m}} - \frac{\nu_{yx,m}}{E_{y,m}} - \frac{\nu_{zy,m}}{E_{z,m}}\right)}{\left(\frac{1}{E_{x,m}} + \frac{1}{E_{y,m}} + \frac{1}{E_{z,m}} - \frac{2\nu_{yx,m}}{E_{y,m}} - \frac{2\nu_{xz,m}}{E_{x,m}} - \frac{2\nu_{zy,m}}{E_{z,m}}\right)} = \varepsilon_s\frac{p}{p+p_{mL}}\frac{\left(\frac{1}{E_{y,b}} - \frac{\nu_{yx,b}}{E_{y,b}} - \frac{\nu_{zy,b}}{E_{z,b}}\right)}{\left(\frac{1}{E_{x,b}} + \frac{1}{E_{y,b}} + \frac{1}{E_{z,b}} - \frac{2\nu_{yx,b}}{E_{y,b}} - \frac{2\nu_{xz,b}}{E_{x,b}} - \frac{2\nu_{zy,b}}{E_{z,b}}\right)}, \tag{40}$$

$$\varepsilon_{msz} = \varepsilon_s\frac{p}{p+p_{mL}}\frac{\left(\frac{1}{E_{z,m}} - \frac{\nu_{xz,m}}{E_{x,m}} - \frac{\nu_{yz,m}}{E_{y,m}}\right)}{\left(\frac{1}{E_{x,m}} - \frac{\nu_{yx,m}}{E_{y,m}} - \frac{\nu_{zx,m}}{E_{z,m}} + \frac{1}{E_{y,m}} - \frac{\nu_{xy,m}}{E_{x,m}} - \frac{\nu_{zy,m}}{E_{z,m}} + \frac{1}{E_{z,m}} - \frac{\nu_{xz,m}}{E_{x,m}} - \frac{\nu_{yz,m}}{E_{y,m}}\right)} = \varepsilon_s\frac{p}{p+p_{mL}}$$

$$\frac{\left(\frac{1}{E_{z,m}}-\frac{v_{xz,m}}{E_{x,m}}-\frac{v_{zy,m}}{E_{z,m}}\right)}{\left(\frac{1}{E_{x,m}}+\frac{1}{E_{y,m}}+\frac{1}{E_{z,m}}-\frac{2v_{yx,m}}{E_{y,m}}-\frac{2v_{xz,m}}{E_{x,m}}-\frac{2v_{zy,m}}{E_{z,m}}\right)}=\varepsilon_s\frac{p}{p+p_{mL}}\frac{\left(\frac{1}{E_{z,b}}-\frac{v_{xz,b}}{E_{x,b}}-\frac{v_{zy,b}}{E_{z,b}}\right)}{\left(\frac{1}{E_{x,b}}+\frac{1}{E_{y,b}}+\frac{1}{E_{z,b}}-\frac{2v_{yx,b}}{E_{y,b}}-\frac{2v_{xz,b}}{E_{x,b}}-\frac{2v_{zy,b}}{E_{z,b}}\right)}. \quad (41)$$

The above directional linear swelling strains are for matrix blocks. The anisotropic matrix swelling strain and the anisotropic fracture (cleat) swelling strain satisfy the following relation according to Zhou et al. [46]:

$$\varepsilon_{fsy}=\frac{\Delta b_{face}}{b_{face0}}=-\frac{f\Delta L_{faces}}{b_{face0}}=-\frac{fL_{face0}\varepsilon_{msy}}{b_{face0}}=-\frac{f\left(L_{face0}/a_{face0}\right)\varepsilon_{msy}}{\left(b_{face0}/a_{face0}\right)}=-\frac{f(1-\phi_{face0})\varepsilon_{msy}}{\phi_{face0}}, \quad (42)$$

where L_{face0} is the initial side length of the matrix block (m), and ΔL_{faces} is the sorption-induced matrix size increment (m). Here, f is an internal swelling factor (0 to 1), representing the proportion of matrix-swelling-induced deformation that purely contributes to fracture (cleat) aperture variation [30,31,46]. The negative sign indicates that matrix internal swelling narrows the fracture (cleat) aperture. Integrating Eq. 31 yields

$$\frac{\phi_{face}}{\phi_{face0}}=\exp\left[(1-R_c)\frac{\Delta\sigma_{ey}}{E_{y,b}}-(\nu_{xy,b}-\eta_{xy,c}R_c)\frac{\Delta\sigma_{ex}}{E_{x,b}}-(\nu_{zy,b}-\eta_{zy,c}R_c)\frac{\Delta\sigma_{ez}}{E_{z,b}}+\Delta\varepsilon_{fsy}\right]. \quad (43)$$

Substituting Eq. 42 into Eq. 43 yields

$$\frac{\phi_{face}}{\phi_{face0}}=\exp\left[(1-R_c)\frac{\Delta\sigma_{ey}}{E_{y,b}}-(\nu_{xy,b}-\eta_{xy,c}R_c)\frac{\Delta\sigma_{ex}}{E_{x,b}}-(\nu_{zy,b}-\eta_{zy,c}R_c)\frac{\Delta\sigma_{ez}}{E_{z,b}}-\frac{f(1-\phi_{face0})}{\phi_{face0}}\Delta\varepsilon_{msy}\right]=\exp$$
$$\left[(1-R_c)\frac{\Delta\sigma_{ey}}{E_{y,b}}-\beta_{face}\frac{\Delta\sigma_{ex}}{E_{x,b}}-\gamma_{face}\frac{\Delta\sigma_{ez}}{E_{z,b}}-\frac{f(1-\phi_{face0})}{\phi_{face0}}\Delta\varepsilon_{msy}\right]. \quad (44)$$

Here, β and γ are two constants obtained from experimental data fitting. Recalling Eq. 1, the face cleat aperture ratio is

$$\frac{b_{face}}{b_{face0}}=\frac{\phi_{face}\ a_{face}}{\phi_{face0}a_{face0}}\approx\frac{\phi_{face}}{\phi_{face0}}. \quad (45)$$

Similarly, for butt cleats and bedding planes, the porosity ratios and aperture ratios are

$$\frac{\phi_{butt}}{\phi_{butt0}}=\exp\left[(1-R_c)\frac{\Delta\sigma_{ex}}{E_{x,b}}-(\nu_{yx,b}-\eta_{yx,c}R_c)\frac{\Delta\sigma_{ey}}{E_{y,b}}-(\nu_{zx,b}-\eta_{zx,c}R_c)\frac{\Delta\sigma_{ez}}{E_{z,b}}-\frac{f(1-\phi_{butt0})}{\phi_{butt0}}\Delta\varepsilon_{msx}\right]=\exp$$
$$\left[(1-R_c)\frac{\Delta\sigma_{ex}}{E_{x,b}}-\beta_{butt}\frac{\Delta\sigma_{ey}}{E_{y,b}}-\gamma_{butt}\frac{\Delta\sigma_{ez}}{E_{z,b}}-\frac{f(1-\phi_{butt0})}{\phi_{butt0}}\Delta\varepsilon_{msx}\right], \quad (46)$$

$$\frac{\phi_{bed}}{\phi_{bed0}} = \exp\left[(1-R_c)\frac{\Delta\sigma_{ez}}{E_{z,b}} - (\nu_{xz,b} - \eta_{xz,c}R_c)\frac{\Delta\sigma_{ex}}{E_{x,b}} - (\nu_{yz,b} - \eta_{yz,c}R_c)\frac{\Delta\sigma_{ey}}{E_{y,b}} - \frac{f(1-\phi_{bed0})}{\phi_{bed0}}\Delta\varepsilon_{msz}\right] = \exp\left[(1-R_c)\frac{\Delta\sigma_{ez}}{E_{z,b}} - \beta_{bed}\frac{\Delta\sigma_{ex}}{E_{x,b}} - \gamma_{bed}\frac{\Delta\sigma_{ey}}{E_{y,b}} - \frac{f(1-\phi_{bed0})}{\phi_{bed0}}\Delta\varepsilon_{msz}\right], \quad (47)$$

$$\frac{b_{butt}}{b_{butt0}} = \frac{\phi_{butt}\ a_{butt}}{\phi_{butt0}a_{butt0}} \approx \frac{\phi_{butt}}{\phi_{butt0}}, \quad (48)$$

$$\frac{b_{bed}}{b_{bed0}} = \frac{\phi_{bed}\ a_{bed}}{\phi_{bed0}a_{bed0}} \approx \frac{\phi_{bed}}{\phi_{bed0}}. \quad (49)$$

From Eqs. 44 to 49, the porosity ratios and dynamic fracture (cleat) aperture can be obtained so that one can calculate $k_{face,bapp}$, $k_{butt,bapp}$, and $k_{bed,bapp}$. Consequently, the anisotropic permeability k_x, k_y, and k_z are obtained.

3. Model validation

Both the anisotropic swelling model and the anisotropic permeability model are validated by comparing with experimental data. The reliability of the anisotropic swelling model is checked first. By combining the internal swelling factor [30,31,46], the anisotropic swelling model can be inserted into the new anisotropic permeability model to simulate anisotropic internal swelling/shrinkage. Then, the new anisotropic permeability model is verified against anisotropic permeability measurement data obtained under constant pore (cleat) pressure conditions (cases 1 and 2) and constant confining pressure conditions (cases 3 and 4). Note that it is also applicable to the constant effective stress condition ($\Delta\sigma_e = 0$) if we substitute this condition into the permeability equation.

3.1 Validation of the anisotropic swelling model

Coal swelling data reported in the literature [47] are used for anisotropic swelling model validation. The two test pieces were made from an Australian bituminous coal sample [47]. One test piece's long axis is parallel to bedding planes, while the second piece's long axis is perpendicular to bedding planes. The test pieces were degassed before starting swelling strain measurement and injecting CO_2. During the measurement procedure, the pressure gradually increased to 15 MPa, while the temperature was kept constant through water bath [47]. The mechanical and swelling properties used for model validation are: $E_{x,b} = 4.5$ GPa, $E_{y,b} = 4$ GPa, $E_{z,b} = 3.5$ GPa, $\nu_{xz,b} = 0.3$, $\nu_{yx,b} = 0.25$, $\nu_{zy,b} = 0.28$, $p_L = 3$ MPa, and $\varepsilon_s = 0.025$. They are selected based on the literature [44,48,49]. Eqs.39 to 41 are used to calculate swelling strains. Note that the swelling strains parallel to bedding planes usually have marginal difference between each other compared with the swelling strain perpendicular to bedding planes [7]. Here, the linear swelling strain in the *x* direction is used to represent the swelling strain parallel to bedding planes. The *z*-direction linear swelling strain is utilized to describe the swelling strain perpendicular to bedding. Fig. 3 shows the comparison between model's results and experimental data. A reasonable agreement between model's prediction and laboratory observations has been achieved. The anisotropic swelling model is valid for the whole swelling measurement procedure.

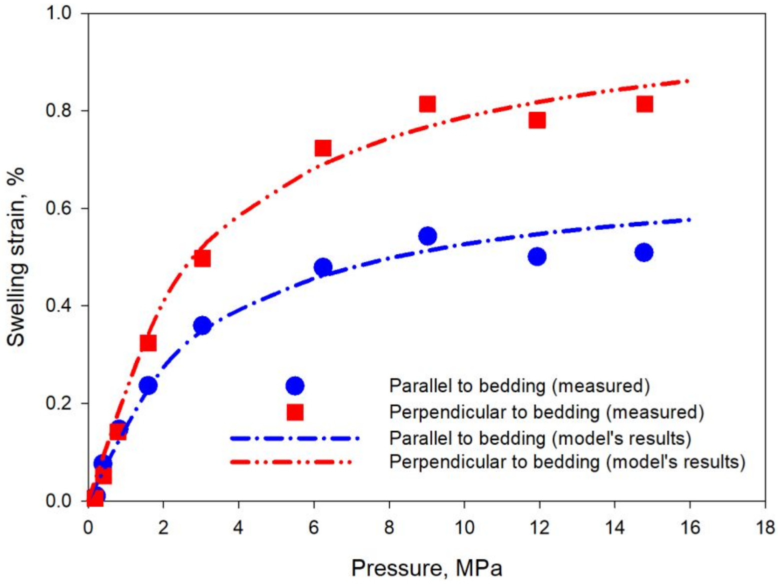

Fig. 3 Comparison of anisotropic swelling data [47] and model's results.

To further check the reliability of the swelling model, swelling data collected from a bituminous coal sample from the Hunter Valley, New South Wales, Australia with CO_2, methane, and nitrogen adsorption respectively [6] were compared with model's results. The mechanical and swelling properties used for model validation are: $E_{x,b} = 4.5$ GPa, $E_{y,b} = 4.4$ GPa, $E_{z,b} = 3.4$ GPa, $\nu_{xz,b} = 0.32$, $\nu_{yx,b} = 0.26$, and $\nu_{zy,b} = 0.29$. For different types of gas, the mechanical properties are the same, but the Langmuir pressure and the swelling strain constant are different: $p_L = 2.8$ MPa and ε_s

$= 0.025$ for CO_2; $p_L = 3.4$ MPa and $\varepsilon_s = 0.0125$ for methane; and $p_L = 4$ MPa and $\varepsilon_s = 0.0055$ for nitrogen. This is because the adsorbability of CO_2 is the strongest, while nitrogen has the lowest adsorbability. The above parameters are reasonable compared with those reported in the literature [44,48,49]. Here, the y-direction linear swelling strain represents the swelling strain parallel to bedding, while the z-direction linear swelling strain is the swelling strain perpendicular to bedding. As can be seen in Figs. 4 and 5, in general, model's prediction matches well with laboratory data, which further confirms the reliability of the anisotropic swelling model.

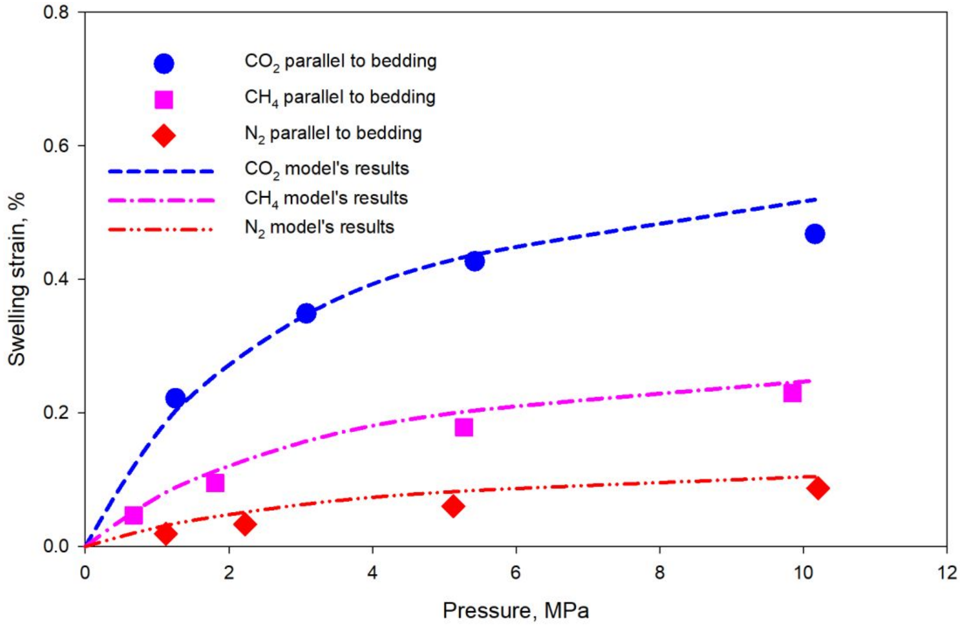

Fig. 4 Comparison of swelling data parallel to bedding upon CO_2, methane, and nitrogen adsorption [6] and model's results.

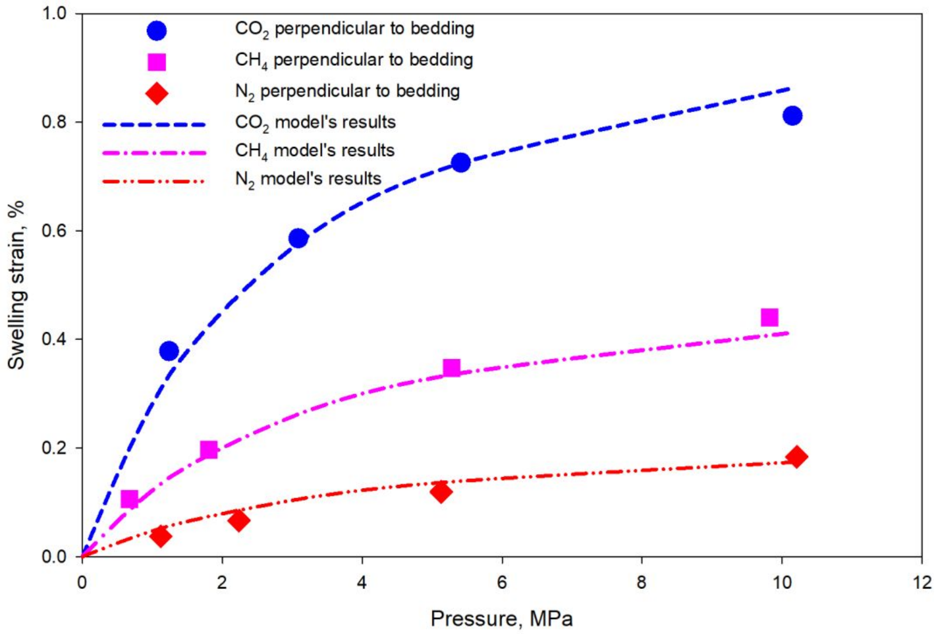

Fig. 5 Comparison of swelling data perpendicular to bedding upon CO_2, methane, and nitrogen adsorption [6] and model's results.

3.2 Validation of the permeability model under constant average pore (fracture) pressure conditions

Permeability measurement data used for anisotropic permeability model validation are also from the literature [50]. For case 1 (constant pore pressure), the cubic coal sample was cut from a coal block in the northern Bowen Basin, Queensland, and the coal rank is relatively low [50,51]. In the permeability measurement procedure, horizontal direction 1 refers to the face cleat direction (x-direction), while horizontal direction 2 is the butt cleat direction (y-direction) [50]. Methane was injected as the flowing fluid. The conceptual model in Fig. 1 is used as an equivalent structure for the real coal sample with more complex and irregular fractures (cleats). The permeability values in the three directions were measured at approximately the same pore (fracture) pressure and effective stress. Here, cubic matrix blocks are applied, and the permeability differences among different directions come from the flow channel aperture, connectivity, and tortuosity. Since no temperature data are available, room temperature (20 °C) is used here. Within the range of common room temperature values, the change of temperature has no noticeable influence on permeability [38]. The basic parameters of the permeability model are [44,48,50,52,53]: $E_{x,b} = 3.6$ GPa, $E_{y,b} = 3.2$ GPa, $E_{z,b} = 2.9$ GPa, $\nu_{yx,b} = 0.31$, $\nu_{zy,b} = 0.35$, $\nu_{xz,b} = 0.33$, $R_C = 300$, $\varepsilon_s = 0.04$, and $p_{mL} = 3$ MPa. Other parameters used in the model are shown in Fig. 6 and are reasonable compared with those in the literature (flow channel aperture [54–56], the tortuosity correction coefficient [56], and the internal swelling factor [31]). The initial flow channel aperture and spacing are determined by matching with initially measured permeability data [50]. These flow channels are equivalent flow channels representing the complex fracture (cleat) system of the sample. Fig. 6 shows that model's results are in good agreement with measured permeability data. The model successfully replicates the permeability evolution behavior in all three directions. Measured permeability in the three directions changes from 0.09 mD to 1.9 mD and exhibits strong anisotropy. As expected, permeability decreases with the increase of effective stress in all three directions. Permeability in horizontal direction 1 (x-direction) is noticeably higher than that in horizontal direction 2 (y-direction). Normally, horizontal permeability is larger than vertical permeability [57]. Interestingly, the vertical permeability here is larger than the permeability in horizontal direction 2. The reason is that the cleats in the vertical direction are better connected compared with those in horizontal direction 2, which is evidenced by micro-CT images of the sample [50].

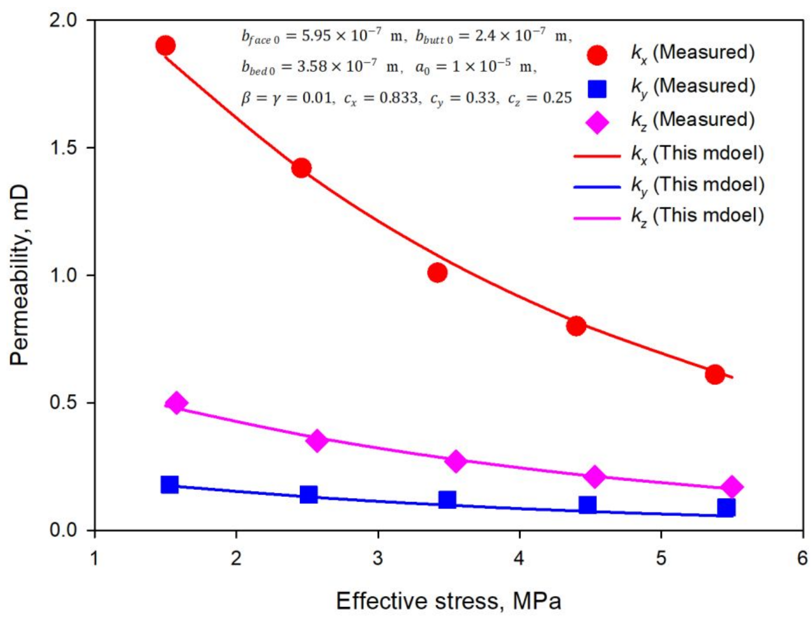

Fig. 6 Comparison between model's results and permeability measurement data from Tan et al. [50] at fixed average pore (fracture) pressure.

In the second case (case 2), the literature-reported permeability data of a low-rank coal sample (sample LY3) collected from the Fukang mining area in the Junggar Basin, China [58], are used to verify the permeability model. Similar to the previous case, the *x*-direction is the face cleat direction, the *y*-direction is for the butt cleat direction, and the *z*-direction refers to the direction perpendicular to bedding. During the permeability measurement process, helium was injected as the testing gas under a constant temperature condition (35℃) [58]. The impact of swelling here is negligible [59]. The average pore pressure (half of the sum of inlet gas pressure and outlet gas pressure) was fixed at 1.55 MPa, while the confining pressure gradually increased. The basic parameters used in the permeability model are [44,48,50,52,53] $E_{x,b} = 3.5$ GPa, $E_{y,b} = 3$ GPa, $E_{z,b} = 2.8$ GPa, $\nu_{yx,b} = 0.28$, $\nu_{zy,b} = 0.33$, $\nu_{xz,b} = 0.31$, and $R_C = 150$. Other parameters, which are reasonable compared with the literature [31,54–56], are listed in Fig. 7. In general, model's results match well with the experimental data (see Fig. 7). In all directions, the permeability declines with effective stress increasing. As normally expected, the permeability parallel to bedding is larger than that perpendicular to bedding. Moreover, the *x*-direction permeability is the highest. The overall permeability of case 2 is smaller than that of case 1.

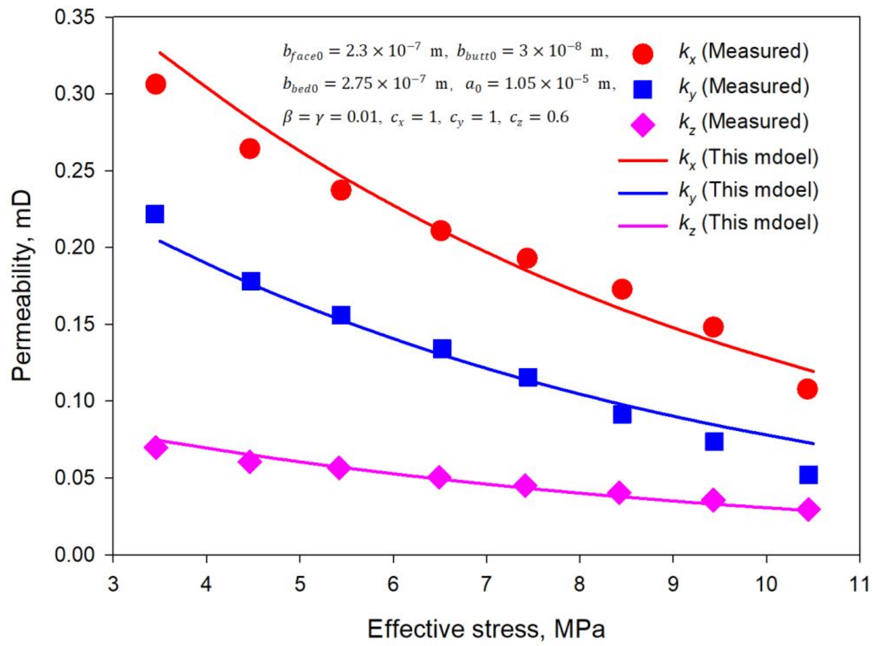

Fig. 7 Comparison between model's results and permeability measurement data from Wang et al. [58] at fixed average pore (fracture) pressure.

3.3 Validation of the permeability model under constant confining pressure conditions

In the third case of permeability model validation (case 3), the permeability data were obtained under constant confining pressure conditions [59]. This permeability test condition tends to be closer to field gas production or injection conditions where reservoir pressure changes with constant overburden pressure. The high-rank coal sample was collected from the Qinshui Basin, China (sample H) [59]. Three cylindrical cores were cut from the same coal sample to investigate permeability anisotropy. The three cores are parallel to face cleats (*x*-direction), parallel to butt cleats (*y*-direction), and perpendicular to bedding planes (*z*-direction) respectively. Helium gas was injected as the flowing fluid so that the impact of swelling is negligible [59]. The confining pressure was fixed at 8 MPa, while the pore (fracture) pressure changed from 4.5 MPa to 2 MPa. The basic parameters of the permeability model are selected according to the literature [44,48,50,52,53]: $E_{x,b} = 3.4$ GPa, $E_{y,b} = 5$ GPa, $E_{z,b} = 3.7$ GPa, $\nu_{yx,b} = 0.34$, $\nu_{zy,b} = 0.32$, $\nu_{xz,b} = 0.31$, and $R_C = 300$. Other parameters used in the model are listed in Fig. 8 and are reasonable compared with the literature [54–

56]. Fig. 8 shows the comparison between experimental data and model's results. Under constant confining pressure conditions, permeability declines with the reduction of pore (fracture) pressure due to the effective stress increment. Our results match well with the measured permeability data. Once again, permeability evolution exhibits strong anisotropy. The overall permeability values in this case are lower than those of case 1. The permeability values in the two horizontal directions are higher than the vertical permeability, which is in accordance with our common knowledge. Since the permeability in the y-direction is the most stress-sensitive with a permeability ratio of 0.61 at 2 MPa, and the permeability in the x-direction is the least stress-sensitive with a permeability ratio of 0.705 at 2 MPa, the deformability of the rock in the three direction has the following order: $x > z > y$. Although the deformability in the vertical direction may usually be larger than the horizontal one, coal deformability (compressibility) orders similar to this case have been reported in the literature as well [26].

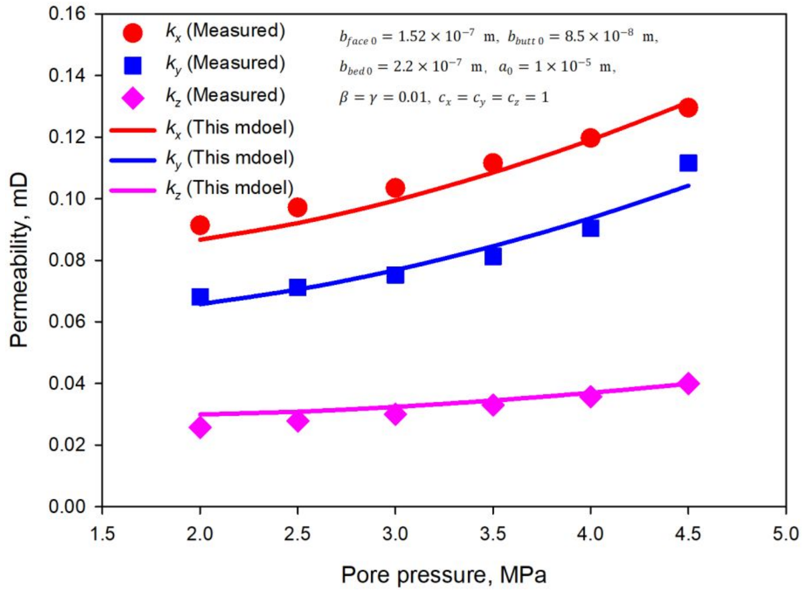

Fig. 8 Comparison between model's results and permeability measurement data from Liu et al. [59] at fixed confining pressure (sample H).

The fourth case is also a constant confining pressure case involving another sample (sample G) from the Qinshui Basin (case 4) [59]. Once again, the three flow directions (x, y, and z) for permeability measurement are parallel to face cleats, parallel to butt cleats, and perpendicular to bedding respectively. Similar to case 3, the pore pressure also changed from 4.5 MPa to 2 MPa, but the confining pressure was smaller (fixed at 7 MPa) with helium injection [59]. The parameters used in the permeability model are [44,48,50,52,53]: $E_{x,b} = 3.2$ GPa, $E_{y,b} = 3.7$ GPa, $E_{z,b} = 3$ GPa, $\nu_{yx,b} = 0.33$, $\nu_{zy,b} = 0.3$, $\nu_{xz,b} = 0.31$, and $R_C = 360$. Other parameters are listed in Fig. 9 and are reasonable compared with those in the literature [54–56]. It can be seen from Fig. 9 that model's results and experimental data show a good agreement, which further demonstrates the reliability of the permeability model. The permeability continuously decreases as pore pressure becomes smaller. The permeability values in the two horizontal directions are close to each other and are larger than the vertical permeability under the same pressure condition. In all the three directions, the permeability of case 4 is more stress-sensitive than that of case 3. The horizontal permeability is more sensitive to the pore pressure change compared with the vertical one.

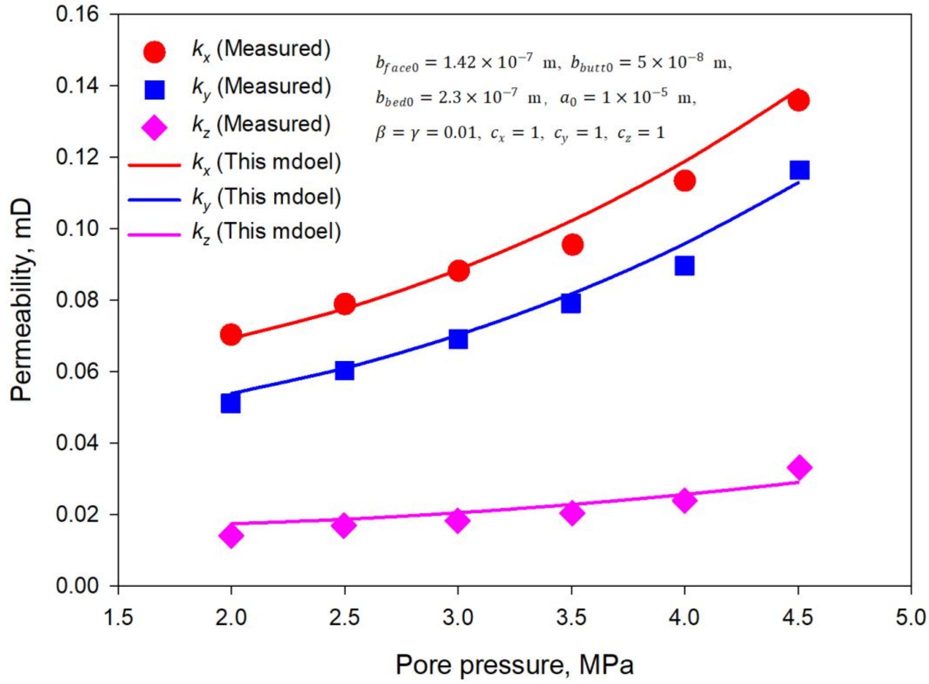

Fig. 9 Comparison between model's results and permeability measurement data from Liu et al. [59] at fixed confining pressure (sample G).

In essence, gas transport in different ranks of coal all involves the basic mechanisms we considered in the proposed permeability model. The differences come from coal's swelling ability, mechanical properties, flow channel aperture, and flow channel spacing due to coal's different composition (different ranks). Accordingly, the magnitudes of stress sensitivity, matrix anisotropic internal swelling/shrinkage, and gas rarefaction effects of different ranks of coal are divergent. This permeability model's applicability to different ranks of coal can be guaranteed through the following factors:

First of all, for the swelling model, there is a generic linear relationship between sorption-induced volumetric strain and adsorbed gas content for different coal rocks and even shale [32,55,60–65]. This relationship is described by the Langmuir-type equation as mentioned in model development: $\varepsilon_{msV} = \varepsilon_{ms}\left[p/(p + p_{mL})\right]$. For different ranks of coal rocks, their degree of swelling and their fracture spacing are dependent on their ranks [66]. As the rank increases, coal's adsorption capacity becomes larger, but the Langmuir-type equation for sorption-induced swelling is still valid [60,66]. Moreover, the results of Zhi et al. [67] indicate that the calculation results of the Langmuir-type equation also match well with coal's volumetric swelling strain generated by supercritical CO_2 adsorption. Note that the inputs of the Langmuir-type equation here are different from those for gaseous CO_2 adsorption [55,67]. Therefore, the swelling model used in the proposed permeability model is applicable to different ranks of coal.

Secondly, for the permeability model, the sugar-cube conceptual model used to develop the permeability model can equivalently represent both coal and shale [23,38]. For different ranks of coal, apart from the above-mentioned swelling ability, the mechanical properties and flow channel spacing are different [48,66]. With the coal rank increasing, Young's modulus turns larger [48], while the flow channel spacing decreases with the coal rank increasing from subbituminous coal to anthracite [66]. In terms of the flow channel size, the narrower the flow channel is, the stronger the gas rarefaction effects would be at low pore pressure. The Beskok-Karniadakis model [28] used in our permeability model can deal with full-range gas flow from continuum flow to free molecular flow. The variation of mechanical properties, flow channel spacing, and flow channel size has no influence on the validity of the conceptual model in representing coal rocks and developing the permeability model. This permeability model is applicable for simulating permeability evolution of different ranks of coal by using certain input parameters.

Based on the above analyses, the developed model is capable of describing anisotropic swelling and anisotropic permeability evolution of coal. Since coal and shale share many similarities, such as gas adsorption, stress sensitivity, and gas rarefaction effects in narrow flow channels [68], the proposed permeability model can be used to simulate shale anisotropic permeability evolution behavior. One can use three sets of equivalent fractures to represent shale fracture (pore) networks. Normally, coal's organic content is larger than that of shale. Thus, the gas-sorption-induced swelling ability of shale is weaker than that of coal. Besides, the flow channel size and mechanical properties of shale are also different from that of coal.

4. Results and discussion

Based on the developed coal permeability model, a set of sensitivity analyses are conducted to uncover the impacts of anisotropic internal swelling/shrinkage, gas rarefaction effects, and anisotropic mechanical properties on permeability evolution. In the base case, methane is the flowing fluid. Major parameters used in the base case are [30,31,53,69,70]: $E_{x,b} = 4.27$ GPa, $E_{y,b} = 3.8$ GPa, $E_{z,b} = 3$ GPa, $\nu_{yx,b} = 0.33$, $\nu_{zy,b} = 0.35$, $\nu_{xz,b} = 0.34$, $R_C = 300$, $T = 293.15$ K, $\varepsilon_s = 0.038$, $f = 0.45$, and $p_{mL} = 2$ MPa. Fig. 10 presents anisotropic permeability evolution of the base case with pore (fracture) pressure increasing from 2 MPa to 8 MPa at fixed confining pressure (12 MPa). The range of permeability is reasonable compared with measured or reported coal permeability data in the literature [67,71,72]. Similar to many experimental observations [73–75] and theoretical predictions [30,31,44,76], U-shaped permeability evolution behavior can be seen in all the three directions. The U-shaped sections are caused by matrix internal swelling and weakening of gas rarefaction effects due to pore (fracture) pressure increasing. When the pore (fracture) pressure further turns larger, effective stress reduction dominates permeability evolution, resulting in a switch of the permeability evolution trend. Figs. 11(a) and 11(b) show the permeability ratios in different directions during gas injection or depletion. The permeability at initial pressure (2 MPa for injection and 8 MPa for depletion) is used as reference permeability for permeability ratio calculation. The overall shapes of different permeability ratio curves are similar to each other during gas injection and depletion respectively. As for gas injection, the range of the *z*-direction permeability ratio is the smallest because $E_{x,b}$ and $E_{y,b}$ are larger than $E_{z,b}$, making k_z the least stress-sensitive. Another reason is the reduction of gas rarefaction effects because b_{face} and b_{butt} are smaller than b_{bed}. Gas rarefaction effects have a stronger influence on k_z which is offered by face and butt cleats. The final permeability is controlled by combined effects of effective stress reduction and gas rarefaction phenomenon weakening. In terms of gas depletion, the range of the permeability ratio change exhibits the following order: $k_x/k_{x0} > k_y/k_{y0} > k_z/k_{z0}$. At low pore (fracture) pressure, permeability rebound occurs owning to matrix internal shrinkage and gas rarefaction effect enhancement which reopen the flow channels. The smaller the flow channel aperture is, the stronger the influence of internal shrinkage and gas rarefaction effects on permeability will be. The order of final permeability ratios at 2MPa pore (fracture) pressure is: $k_z/k_{z0} > k_y/k_{y0} > k_x/k_{x0}$. Note that this order may change if swelling-related properties are different. The magnitude of internal shrinkage in different directions also controls the final permeability ratio. Even flow channels in the z-direction are narrower than bedding planes, the final value of k_z/k_{z0} could be lower than that of k_y/k_{y0} if internal shrinkage of bedding planes (shrinkage in the z-direction) is notably stronger than that of face and butt cleats. Fig. 12 shows matrix internal swelling strain increments ($f\Delta\varepsilon_{ms}$) in the three directions during gas injection. The *z*-direction swelling strain increment is significantly higher than those in the two horizontal directions. There is only a marginal difference between those in the two horizontal directions. The anisotropic ratios of the strain increments are: 1.135 ($f\Delta\varepsilon_{msx}/f\Delta\varepsilon_{msy}$), 2.023 ($f\Delta\varepsilon_{msz}/f\Delta\varepsilon_{msx}$), and 2.297($f\Delta\varepsilon_{msz}/f\Delta\varepsilon_{msy}$) respectively.

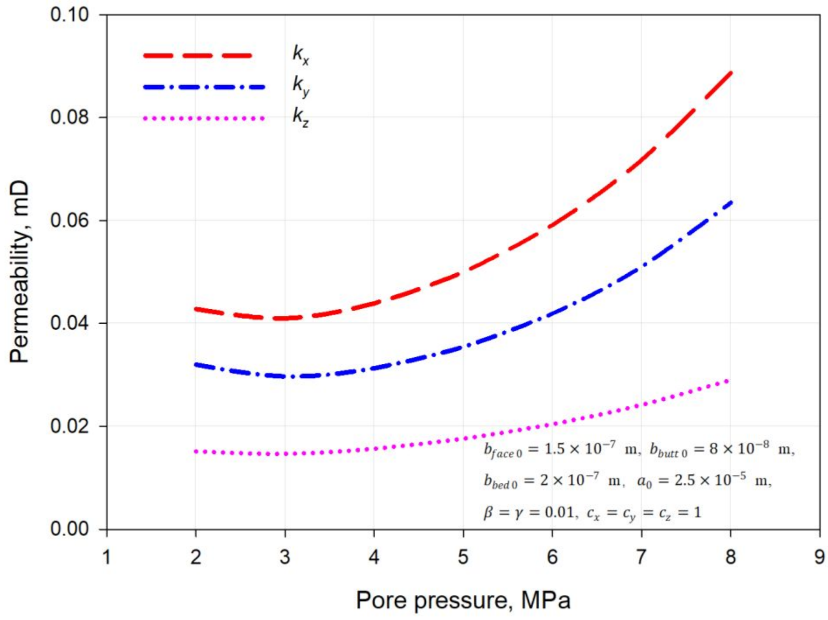

Fig. 10 Anisotropic permeability evolution of the base case.

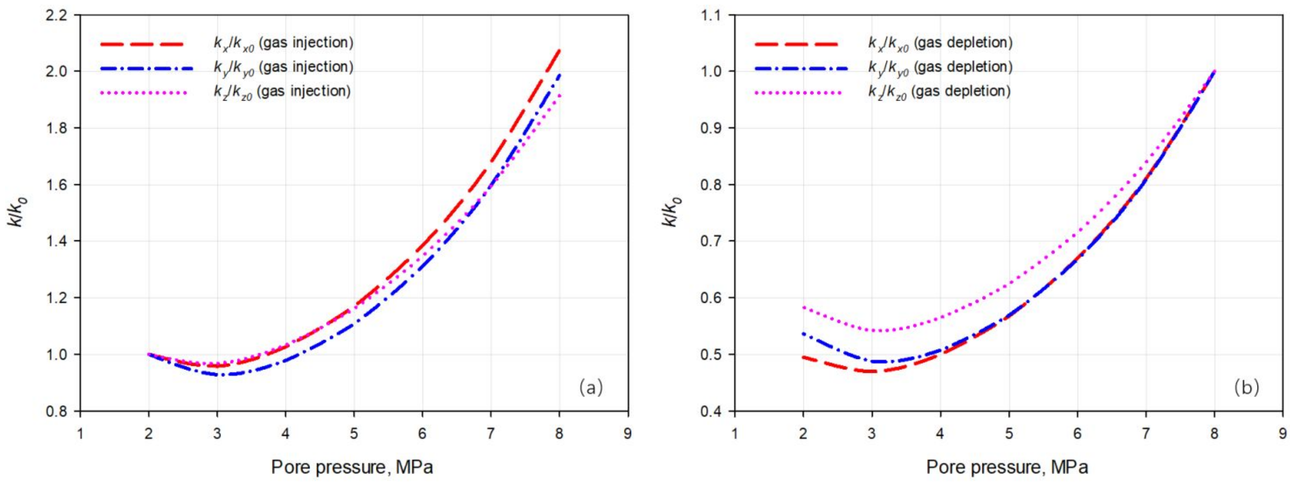

Fig. 11 Permeability ratios of the base case under constant confining pressure conditions: (a) gas injection and (b) gas depletion.

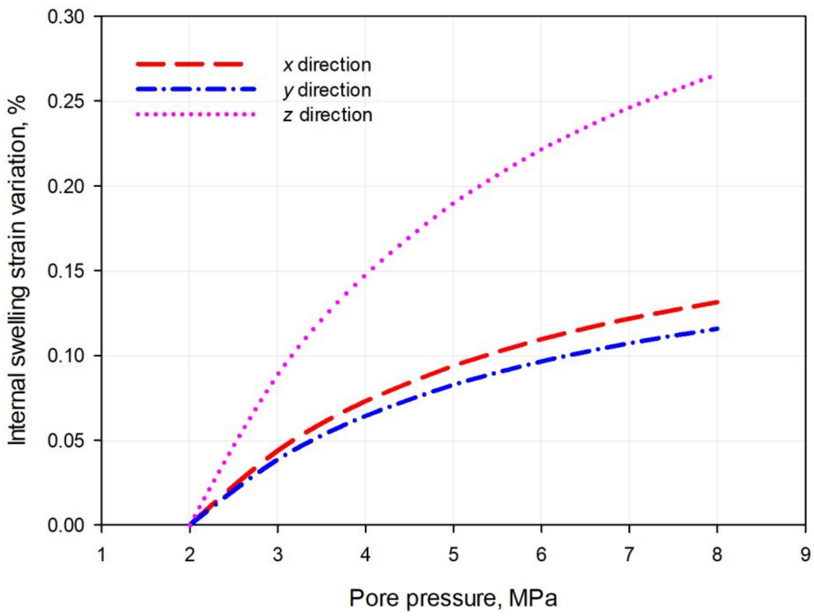

Fig. 12 Internal swelling strain increments in different directions (gas injection).

4.1 Impact of anisotropic internal swelling/shrinkage

Internal swelling/shrinkage refers to the portion of matrix swelling/shrinkage that is near the pore (fracture) surface and purely contributes to fracture deformation (see Fig. 2) [30,31,44]. Since permeability is provided by these flow channels, this swelling/shrinkage phenomenon significantly influences permeability evolution. The anisotropic mechanical properties of coal make internal swelling/shrinkage become anisotropic. Here, how anisotropic internal swelling/shrinkage controls permeability evolution is investigated. The internal swelling strain factor (f) changes from 0 to 0.6. The larger this factor is, a larger proportion of matrix swelling/shrinkage contributes to internal swelling/shrinkage. Figs. 13 and 14 show anisotropic permeability evolution behavior with different internal swelling strain factors. In the two figures, each color represents a group of permeability curves (k_x, k_y, and k_z) calculated with a certain internal swelling factor. As for gas injection, permeability ratio curves for the three directions all move down with f increasing. Meanwhile, the monotonically increasing curves gradually transform into U-shaped curves. The differences among the permeability ratio curves in different directions also become smaller (lower permeability ratio anisotropy level). Among the three directions, k_x/k_{x0} exhibits the most noticeable drop with the increase of f. This is followed by k_y/k_{y0}. The reason is that bedding plane's internal swelling (*z*-direction) is stronger than that of face and butt cleats. Thus, the two horizontal permeability ratios are more sensitive to the change of this internal swelling strain factor. On the contrary, for gas depletion, permeability ratios move upward as f increases. When f reaches 0.45, the permeability rebound at low pore (fracture) pressure in all three directions becomes observable. Once again, the two horizontal permeability ratios are more sensitive to the variation of f. Figs. 15 and 16 compare anisotropic permeability evolution with anisotropic internal swelling/shrinkage and isotropic internal swelling/shrinkage. Note that, in the isotropic internal swelling/shrinkage case, we only use the isotropic internal swelling strain change to replace the anisotropic one, other coal properties are still anisotropic. When internal swelling/shrinkage is simply described by the isotropic swelling/shrinkage model, permeability ratio becomes considerably different. This is because the isotropic internal swelling/shrinkage case underestimates *z*-direction internal swelling/shrinkage that affects k_x and k_y, while *x*- and *y*-direction internal swelling/shrinkage that influences k_z is overestimated. Anisotropic internal swelling/shrinkage controls the shape of permeability evolution curves and the magnitude of permeability ratio variation.

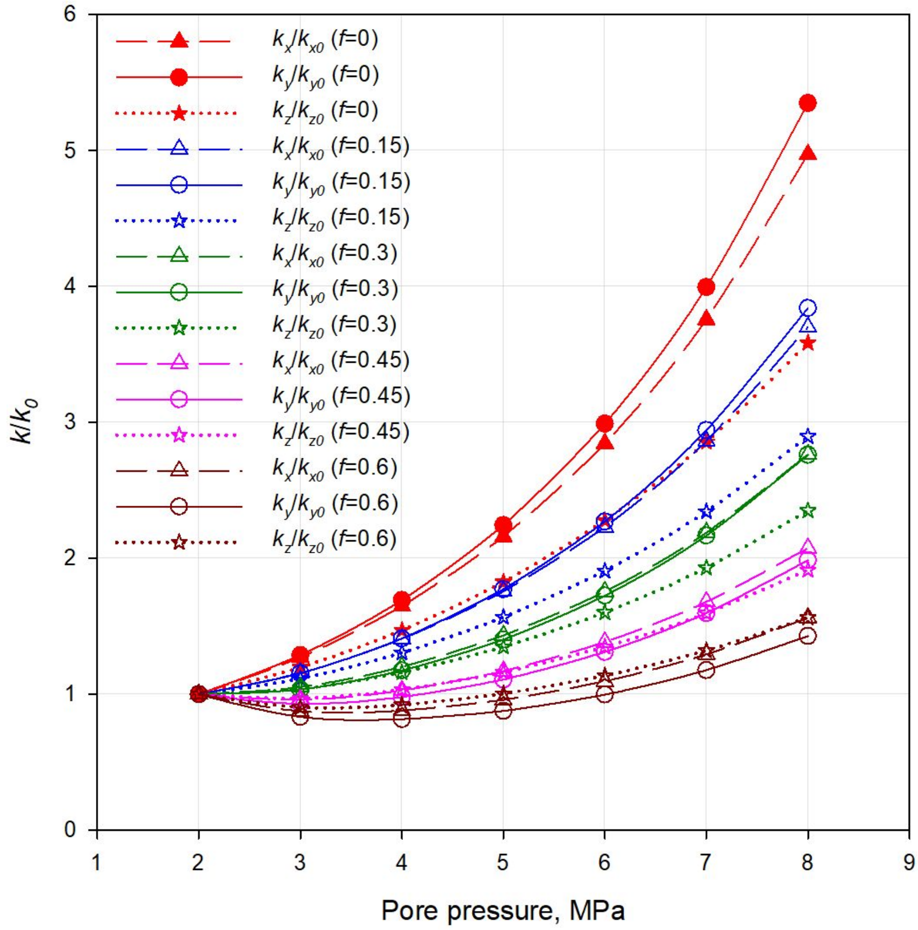

Fig. 13 Comparison of permeability ratios with different internal swelling factors (gas injection).

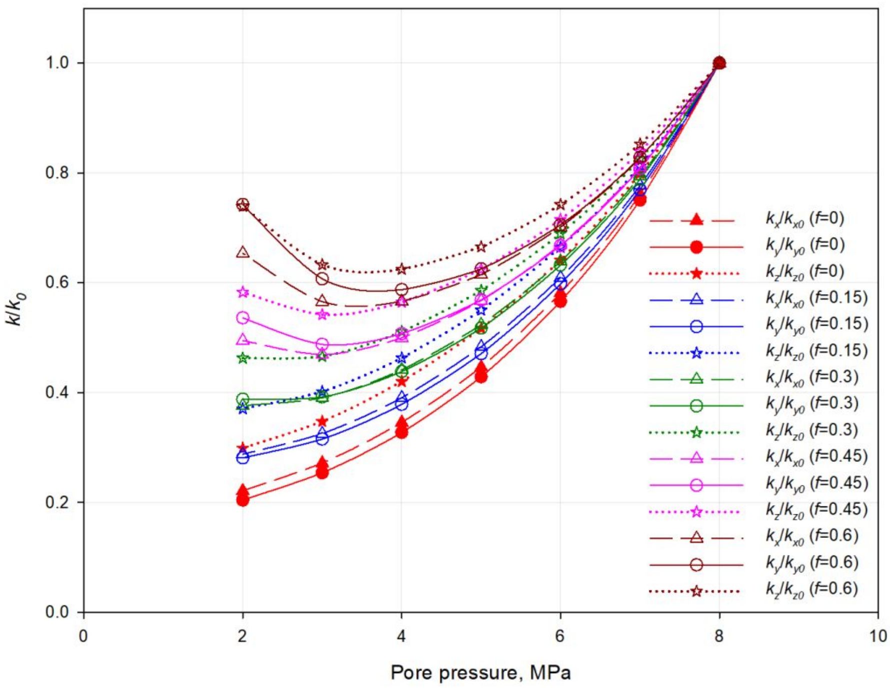

Fig. 14 Comparison of permeability ratios with different internal swelling factors (gas depletion).

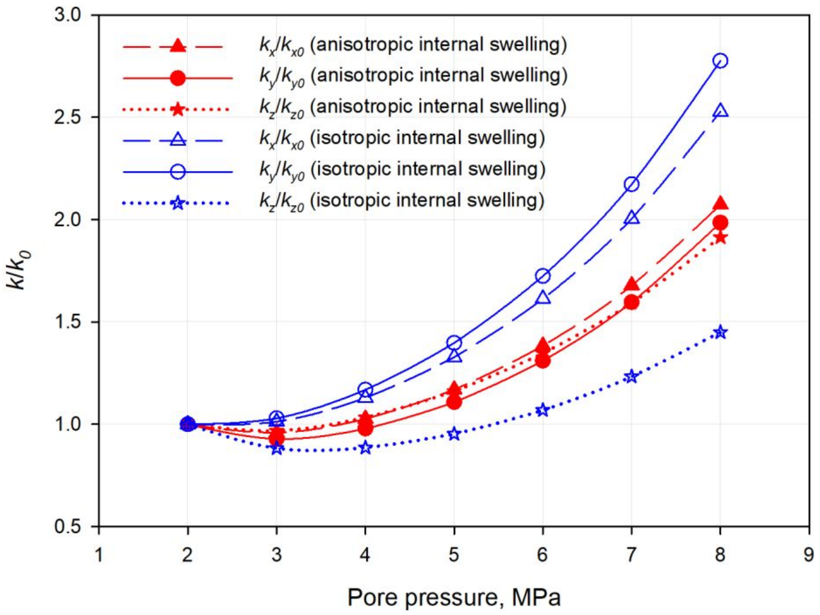

Fig. 15 Comparison of permeability evolution with anisotropic internal swelling and isotropic internal swelling.

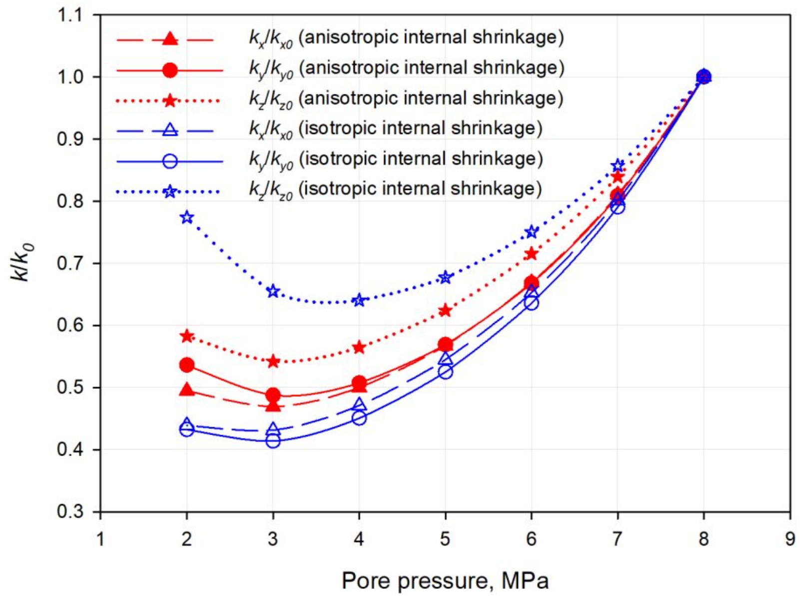

Fig. 16 Comparison of permeability evolution with anisotropic internal shrinkage and isotropic internal shrinkage.

4.2 Impact of gas rarefaction effects

As confirmed by many experimental studies, gas rarefaction effects or gas slippage should be considered when modeling coal permeability evolution [12–14]. Figs. 17 and 18 show anisotropic permeability evolution with and without gas rarefaction effects during gas injection and depletion. The permeability ratios calculated without gas rarefaction effects in all three directions are larger than those consider this phenomenon for gas injection. There is no U-shaped section for the *z*-direction permeability ratio curve. With gas rarefaction effects, when pore (fracture) pressure rises, weakening of gas rarefaction effects generates the U-shaped section or makes the existing sorption-induced U-shaped section more conspicuous. For gas depletion, ignoring gas the rarefaction phenomenon leads to underestimation of permeability, especially at low pore pressure. The gas rarefaction phenomenon enhances the permeability rebound at low pressure in addition to internal shrinkage. Due to the anisotropy of coal, the significance of the impact of this phenomenon on permeability is not identical for different flow directions. The narrower the flow channel is, the more noticeable this impact would be with identical pore (fracture) pressure change. The Knudsen number of flow channels in the three directions ranges from 0.003 to 0.039 during gas injection, and from 0.004 to 0.040 for gas depletion. This indicates that the flow regimes of different cases all fall in the slip flow regime [77]. The impact of gas rarefaction effects on permeability is less noticeable compared with that of anisotropic internal swelling/shrinkage.

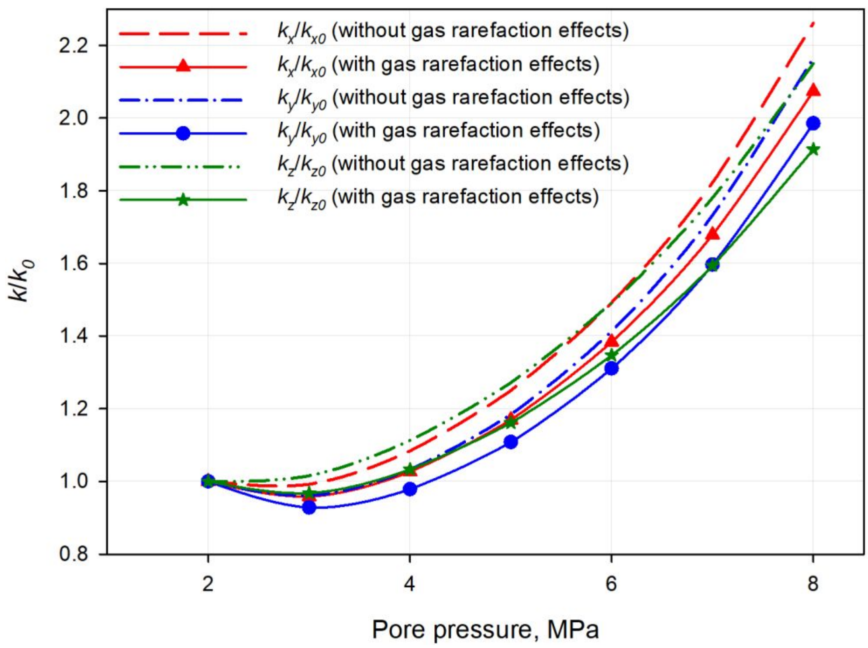

Fig. 17 Comparison of anisotropic permeability evolution with and without gas rarefaction effects (gas injection).

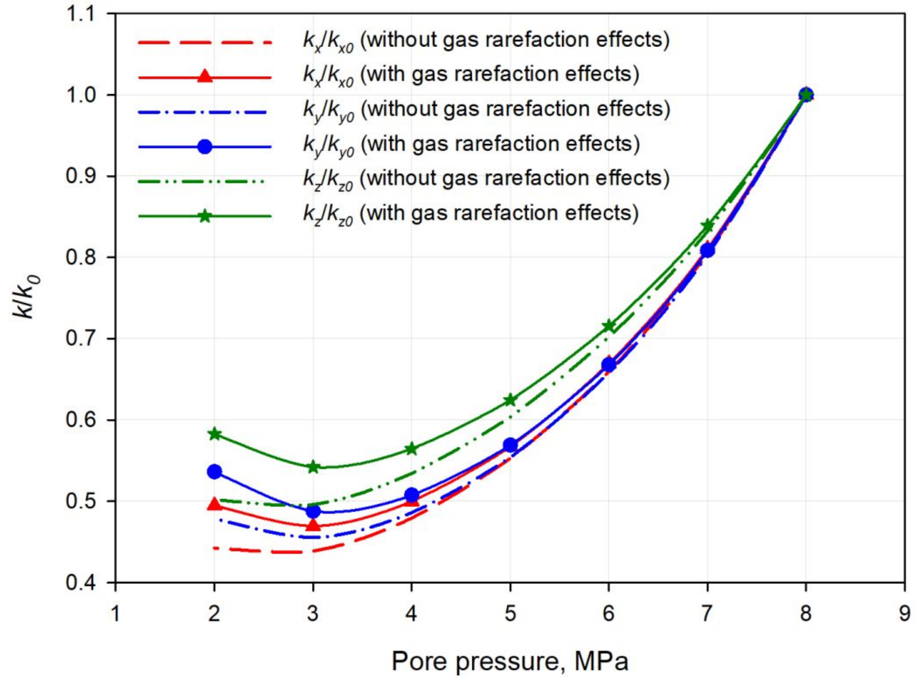

Fig. 18 Comparison of anisotropic permeability evolution with and without gas rarefaction effects (gas depletion).

4.3 Impact of combined effects of internal swelling/shrinkage and the gas rarefaction phenomenon

After understanding the impacts of internal swelling/shrinkage and the gas rarefaction phenomenon on permeability evolution, permeability evolution with and without the combined effects of the two phenomena is analyzed here. As shown in Fig. 19, if we ignore internal shrinkage and gas rarefaction effects during gas injection, the permeability ratios in all three directions are remarkably higher than those with the two phenomena. Unlike the base case, the overall permeability evolution is simply controlled by effective stress so that permeability monotonically increases with pore pressure rising. The order of permeability ratio values reveals the level of stress sensitivity. Fig. 20 demonstrates permeability evolution during gas depletion. Without the two mechanisms, permeability drops monotonically which is analogous to permeability evolution of conventional reservoir rocks. No permeability rebound can be observed. In the process of gas injection, the permeability ratios in *x*, *y*, and *z* directions are 2.63 times, 2.95 times, and 2.11 times the actual ones at 8 MPa pore pressure. For gas extraction, the permeability ratios in *x*, *y*, and *z* directions are only 38%, 32%, and 43% of the actual ones at 2 MPa pore pressure. In general, permeability evolution behavior considerably deviates from that of the base case if both internal swelling/shrinkage and gas rarefaction effects are not incorporated. The two phenomena should be concurrently considered when modeling anisotropic coal permeability evolution.

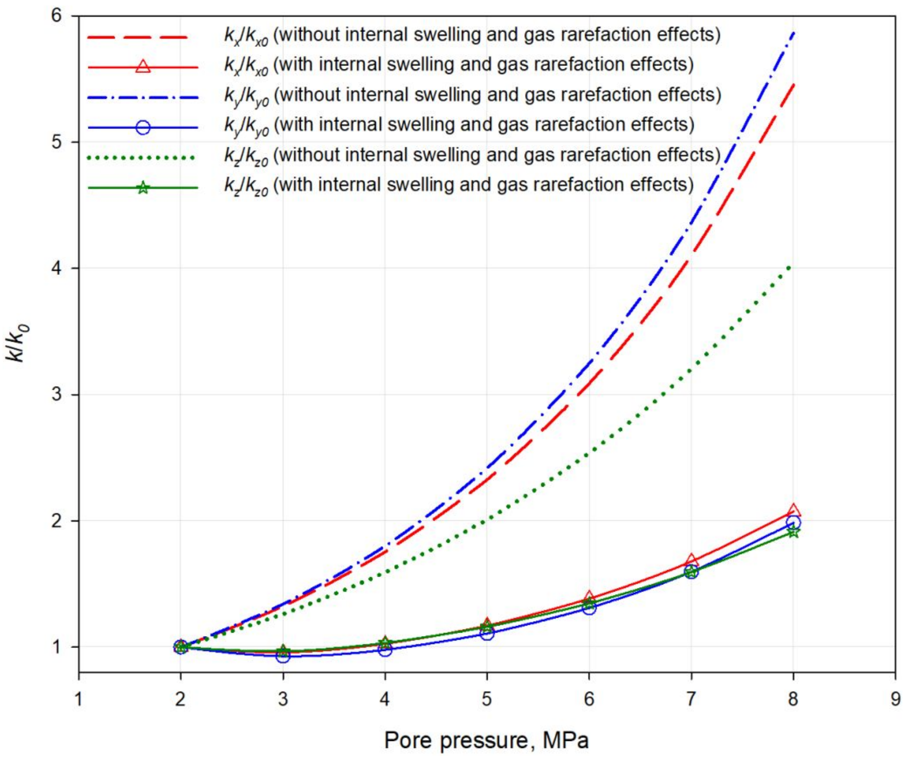

Fig. 19 Comparison of anisotropic permeability evolution with and without the combined effects of internal swelling and the gas rarefaction phenomenon (gas injection).

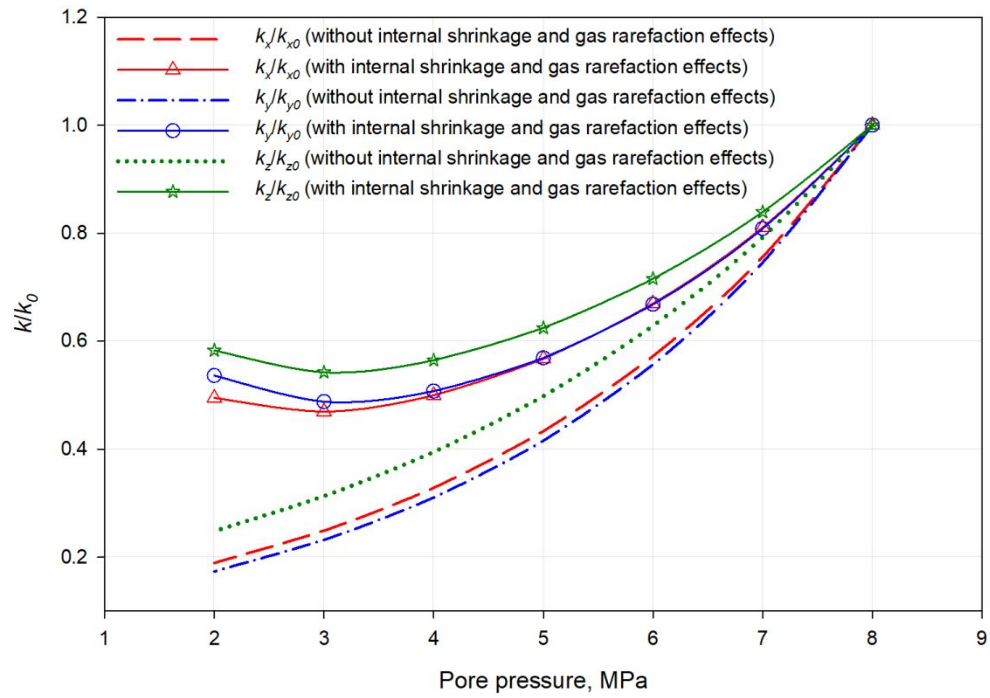

Fig. 20 Comparison of anisotropic permeability evolution with and without the combined effects of internal shrinkage and the gas rarefaction phenomenon (gas depletion).

4.4 Impact of anisotropic mechanical properties

Coal is generally anisotropic so that its properties vary spatially and orientationally [78,79]. Here, we investigate the difference between permeability evolution of the base case and an isotropic-mechanical-property case. Note that the initial permeability is still anisotropic in the isotropic-mechanical-property case where the mechanical property values are the arithmetic average values of those in the base case. Therefore, in the isotropic case, $E_{x,b} = E_{y,b} = E_{z,b} = 3.69$ GPa, and $\nu_{yx,b} = \nu_{zy,b} = \nu_{xz,b} = 0.34$. The swelling behavior of the two cases is analyzed first to help better understand permeability evolution. Fig. 21 shows internal swelling strain increments for anisotropic and isotropic-mechanical-property cases. For the isotropic swelling case, this strain increment is 1/3 of the matrix internal volumetric swelling strain increment according to Eqs. 39 to 41. The isotropic internal swelling increment curve is sandwiched by those of the anisotropic swelling case. The vertical internal swelling strain increment of the anisotropic swelling case is larger than that in the isotropic swelling case, while the two horizontal internal swelling strain increments in the anisotropic swelling case are smaller than the isotropic ones.

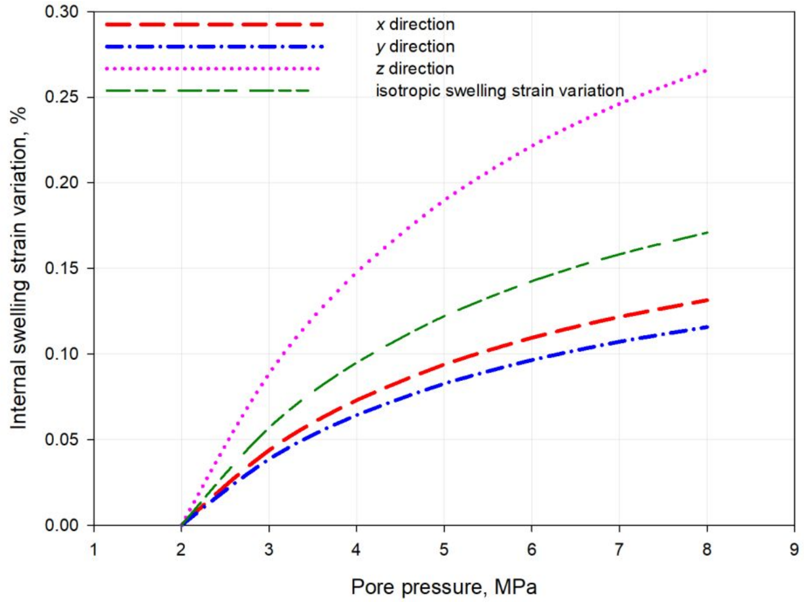

Fig. 21 Comparison of internal swelling strain increments for anisotropic and isotropic swelling cases (gas injection).

Figs. 22 and 23 show permeability evolution of the two cases. The dashed curves represent the permeability ratio of the isotropic-mechanical-property case, while the solid curves with symbols are for those of the anisotropic case. During low-pore-pressure gas injection, the permeability ratios of the anisotropic case in *x* and *y* directions (green and red solid curves) are smaller than those of the isotropic-mechanical-property case. This is because the z-direction internal swelling in the anisotropic case is markedly stronger than that in the isotropic case, resulting in narrower bedding planes and lower horizontal permeability. Bedding planes have the largest aperture and contribute more to horizontal permeability compared with face and butt cleats. In contrast, the vertical permeability ratio of the anisotropic case is higher than that of the isotropic case because swelling in *x* and *y* directions is weaker in the anisotropic case. As fracture (pore) pressure increases, permeability evolution controlling factors gradually transform from internal swelling to the combined influence of internal swelling and coal mechanical properties (stress sensitivity). In terms of gas depletion, with fracture (pore) pressure decreasing, permeability ratios of the isotropic-mechanical-property case are generally larger than the corresponding permeability ratios in the anisotropic case. k_x and k_y are less stress-sensitive in the isotropic-mechanical-property case where $E_{z,b}$ is 23% larger than that in the anisotropic case. The z-direction internal shrinkage of the isotropic case is conspicuously weaker than that of the anisotropic case, although its internal shrinkage in x and y directions is slightly stronger than that of the anisotropic case. Accordingly, the permeability ratios' rebound in x and y direction are more noticeable in the anisotropic case. For vertical permeability, k_z in the isotropic-mechanical-property case should be more stress-sensitive and has a more noticeable decline at low pore pressure because $E_{x,b}$ and $E_{y,b}$ in that case are 13.6% and 2.9% smaller than those in the anisotropic case. However, the reduction of k_z at low pore pressure in the isotropic case is masked by the permeability rebound induced by stronger internal shrinkage in x and y directions compared with the anisotropic case with weaker horizontal internal shrinkage. This leads to a more noticeable vertical permeability ratio rebound for the isotropic case (the green dashed curve). To sum up, the competitive effects of anisotropic deformation caused by effective stress variation, anisotropic internal swelling/shrinkage, and the gas rarefaction phenomenon dominate the overall anisotropic permeability evolution.

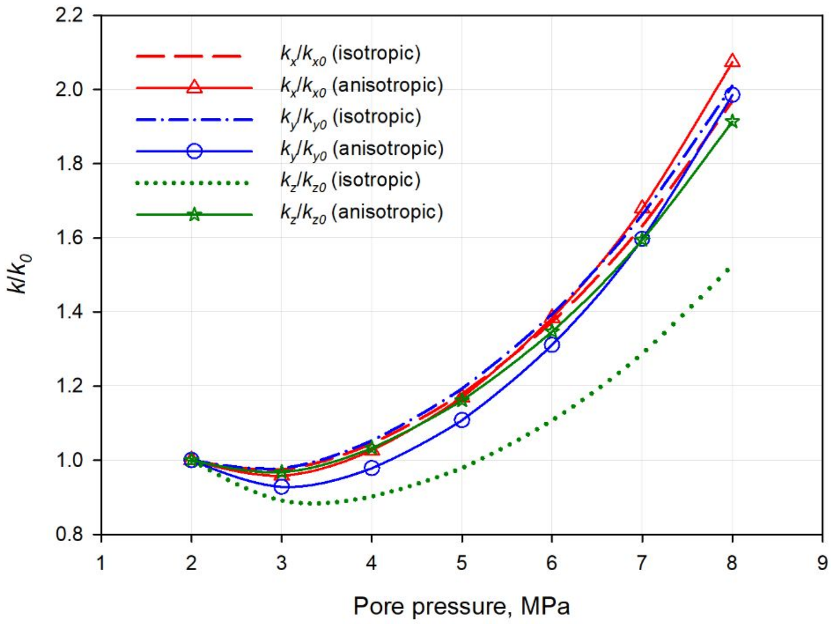

Fig. 22 Comparison of permeability evolution in the isotropic-mechanical-property case and the

anisotropic case (gas injection).

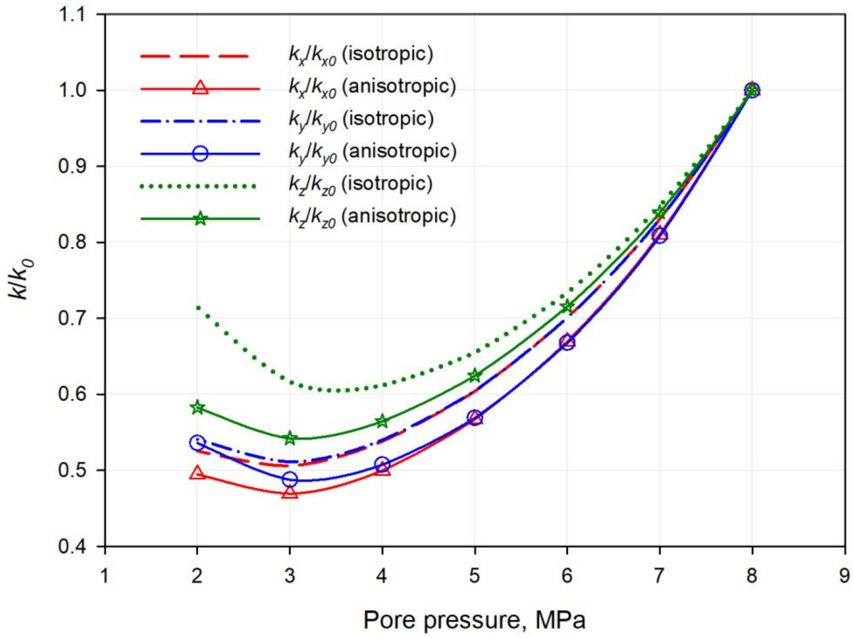

Fig. 23 Comparison of permeability evolution in the isotropic-mechanical-property cases and the anisotropic case (gas depletion).

5. Conclusions

In this research, a mechanical-property-based coal swelling model is proposed to describe anisotropic internal swelling/shrinkage via the energy balance theory. Based on this swelling model and the modified sugar-cube coal conceptual model, a new anisotropic permeability model is developed incorporating the impacts of stress sensitivity, anisotropic internal swelling/shrinkage, and the gas rarefaction phenomenon. The developed permeability model satisfactorily replicates published coal anisotropic permeability evolution data under constant average pore pressure and constant confining pressure conditions. It can also mimic permeability evolution under constant effective stress conditions ($\Delta\sigma_e = 0$). The following key conclusions can be drawn.

(1) Coal anisotropic internal swelling/shrinkage is related to coal's anisotropic mechanical properties. This swelling/shrinkage phenomenon controls the overall shape of anisotropic permeability evolution curves and the magnitude of permeability variation. With the increase of the

internal swelling factor, the permeability ratio curves for gas injection move down, while the curves for gas depletion move upwards. The monotonically increasing/decreasing curves for gas injection/depletion also transform into U-shaped curves gradually. Ignoring anisotropic internal swelling/shrinkage or simply using the isotropic internal swelling/shrinkage model generates significant discrepancy between model results and actual permeability data.

(2) The impact of the gas rarefaction phenomenon is dependent on fracture (pore) pressure and flow channel aperture. During gas injection, weaking of gas rarefaction effects with increasing fracture (pore) pressure makes the actual permeability lower than model prediction without the gas rarefaction phenomenon. For gas depletion, the permeability enhancement caused by the gas rarefaction phenomenon is particularly noticeable at the permeability rebound period. Due to coal's anisotropic feature, the significance of the impact of this phenomenon on permeability evolution is not identical for different flow directions. The narrower the flow channel is, the more noticeable the impact would be with the same fracture (pore) pressure variation. Flow regimes of all the studied cases fall in the slip flow regime. Gas rarefaction phenomenon's impact on permeability evolution is not as strong as that of anisotropic internal swelling/shrinkage.

(3) Permeability evolution in different directions may significantly deviate from each other. The stress sensitivity level in each direction is also affected by the actual mechanical properties. The existence of anisotropic internal swelling/shrinkage and the gas rarefaction phenomenon shows a synergistic effect on anisotropic permeability evolution with fracture (pore) pressure changing. The competitive effects of effective stress variation, anisotropic internal swelling/shrinkage, and the gas rarefaction phenomenon determine the overall anisotropic permeability evolution. Our research provides more comprehensive understanding of coal anisotropic permeability evolution with multiple controlling factors.

Acknowledgements

The authors would like to acknowledge the support of International Postdoctoral Exchange

Fellowship Program (YJ20220169).

References

[1] Liu, X., Sheng, J., Ma, C., Liu, J., & Gao, H. (2020). Complete coal permeability models from initial to ultimate equilibrium. Fuel, 271, 117612.

[2] An, H., Wei, X. R., Wang, G. X., Massarotto, P., Wang, F. Y., Rudolph, V., & Golding, S. D. (2015). Modeling anisotropic permeability of coal and its effects on CO_2 sequestration and enhanced coalbed methane recovery. International Journal of Coal Geology, 152, 15-24.

[3] Liu, Y., Li, M., Yin, G., Zhang, D., & Deng, B. (2018). Permeability evolution of anthracite coal considering true triaxial stress conditions and structural anisotropy. Journal of Natural Gas Science and Engineering, 52, 492-506.

[4] Chen, D., Pan, Z., Liu, J., & Connell, L. D. (2012). Characteristic of anisotropic coal permeability and its impact on optimal design of multi-lateral well for coalbed methane production. Journal of Petroleum Science and Engineering, 88-89, 13-28.

[5] Shi, J. Q., & Durucan, S. (2004). Drawdown induced changes in permeability of coalbeds: a new interpretation of the reservoir response to primary recovery. Transport in porous media, 56(1), 1-16.

[6] Pan, Z., & Connell, L. D. (2011). Modelling of anisotropic coal swelling and its impact on permeability behaviour for primary and enhanced coalbed methane recovery. International Journal of Coal Geology, 85(3-4), 257-267.

[7] Niu, Q., Cao, L., Sang, S., Zhou, X., & Wang, Z. (2018). Anisotropic adsorption swelling and permeability characteristics with injecting CO2 in coal. Energy & fuels, 32(2), 1979-1991.

[8] Wang, J. G., Liu, J., & Kabir, A. (2013). Combined effects of directional compaction, non-Darcy flow and anisotropic swelling on coal seam gas extraction. International Journal of Coal Geology, 109-110, 1-14.

[9] Palmer, I., & Mansoori, J. (1998). How permeability depends on stress and pore pressure in coalbeds: A new model. SPE Reservoir Evaluation & Engineering, 1(06), 539-544.

[10] Wang, L. L., Vandamme, M., Pereira, J. M., Dangla, P., & Espinoza, N. (2018). Permeability changes in coal seams: The role of anisotropy. International Journal of Coal Geology, 199, 52-64.

[11] Seidle, J. R., & Huitt, L. G. (1995). Experimental measurement of coal matrix shrinkage due to gas desorption and implications for cleat permeability increases. In International meeting on petroleum Engineering. Society of Petroleum Engineers.

[12] Meng, Y., Li, Z., & Lai, F. (2021). Influence of effective stress on gas slippage effect of different rank coals. Fuel, 285, 119207.

[13] Li, Y., Tang, D., Xu, H., Meng, Y., & Li, J. (2014). Experimental research on coal permeability: the roles of effective stress and gas slippage. Journal of Natural Gas Science and Engineering, 21, 481-488.

[14] Niu, Y., Mostaghimi, P., Shikhov, I., Chen, Z., & Armstrong, R. T. (2018). Coal permeability: gas slippage linked to permeability rebound. Fuel, 215, 844-852.

[15] Zou, J., Chen, W., Yang, D., Yu, H., & Yuan, J. (2016). The impact of effective stress and gas slippage on coal permeability under cyclic loading. Journal of Natural Gas Science and Engineering, 31, 236-248.

[16] Li, B., Yang, K., Xu, P., Xu, J., Yuan, M., & Zhang, M. (2019). An experimental study on permeability characteristics of coal with slippage and temperature effects. Journal of Petroleum Science and Engineering, 175, 294-302.

[17] Wang, G., Ren, T., Wang, K., & Zhou, A. (2014). Improved apparent permeability models of gas flow in coal with Klinkenberg effect. Fuel, 128, 53-61.

[18] Zhou, Y., Li, H., Huang, J., Zhang, R., Wang, S., Hong, Y., & Yang, Y. (2021). Influence of coal deformation on the Knudsen number of gas flow in coal seams. Energy, 233, 121161.

[19] Letham, E. A., & Bustin, R. M. (2016). The impact of gas slippage on permeability effective stress laws: implications for predicting permeability of fine-grained lithologies. International Journal of Coal Geology, 167, 93-102.

[20] Raza, S. S., Ge, L., Rufford, T. E., Chen, Z., & Rudolph, V. (2019). Anisotropic coal permeability estimation by determining cleat compressibility using mercury intrusion porosimetry and stress–strain measurements. International Journal of Coal Geology, 205, 75-86.

[21] Wu, Y., Liu, J., Elsworth, D., Miao, X., & Mao, X. (2010). Development of anisotropic permeability during coalbed methane production. Journal of Natural Gas Science and Engineering, 2(4), 197-210.

[22] Liu, J., Chen, Z., Elsworth, D., Miao, X., & Mao, X. (2010). Linking gas-sorption induced changes in coal permeability to directional strains through a modulus reduction ratio. International Journal of Coal Geology, 83(1), 21-30.

[23] Wang, K., Zang, J., Wang, G., & Zhou, A. (2014). Anisotropic permeability evolution of coal with effective stress variation and gas sorption: model development and analysis. International Journal of Coal Geology, 130, 53-65.

[24] Moore, R., & Higgs, N. (2015). Anisotropic model for permeability change in coalbed-methane wells. SPE

Reservoir Evaluation & Engineering, 18(04), 456-462.
[25] Zhang, Z., Zhang, R., Xie, H., Gao, M., Zha, E., & Jia, Z. (2017). An anisotropic coal permeability model that considers mining-induced stress evolution, microfracture propagation and gas sorption-desorption effects. Journal of Natural Gas Science and Engineering, 46, 664-679.
[26] Li, J., Li, B., Wang, Z., Ren, C., Yang, K., & Gao, Z. (2021). A permeability model for anisotropic coal masses under different stress conditions. Journal of Petroleum Science and Engineering, 198, 108197.
[27] Klinkenberg, L. J. (1941). The permeability of porous media to liquids and gases. Am. Petrol. Inst., Drilling and Production Practice, 2, 200-213.
[28] Beskok, A., & Karniadakis, G. E. (1999). Report: a model for flows in channels, pipes, and ducts at micro and nano scales. Microscale thermophysical engineering, 3(1), 43-77.
[29] Reiss, L. H. (1980). The reservoir engineering aspects of fractured formations. Editions Technip.
[30] Guo, P., Cheng, Y., Jin, K., Li, W., Tu, Q., & Liu, H. (2014). Impact of effective stress and matrix deformation on the coal fracture permeability. Transport in porous media, 103(1), 99-115.
[31] Liu, H. H., & Rutqvist, J. (2010). A new coal-permeability model: internal swelling stress and fracture–matrix interaction. Transport in Porous Media, 82(1), 157-171.
[32] Cui, X., & Bustin, R. M. (2005). Volumetric strain associated with methane desorption and its impact on coalbed gas production from deep coal seams. AAPG Bulletin, 89(9), 1181-1202.
[33] Li, J., Li, B., Cheng, Q., & Gao, Z. (2022). Characterization of anisotropic coal permeability with the effect of sorption-induced deformation and stress. Fuel, 309, 122089.
[34] van Golf-Racht, T. D. (1982). Fundamentals of fractured reservoir engineering. Elsevier.
[35] Javadpour, F., Fisher, D., & Unsworth, M. (2007). Nanoscale gas flow in shale gas sediments. Journal of Canadian Petroleum Technology, 46(10): 55-61.
[36] Moghadam, A. A., & Chalaturnyk, R. (2016). Analytical and experimental investigations of gas-flow regimes in shales considering the influence of mean effective stress. SPE Journal, 21(02): 557-572.
[37] Pan, Z., & Connell, L. D. (2012). Modelling permeability for coal reservoirs: a review of analytical models and testing data. International Journal of Coal Geology, 92, 1-44.
[38] Zeng, J., Liu, J., & Guo, J. (2022). Characterization of gas transport in shale: A multi-mechanism permeability modeling approach. Chemical Engineering Journal, 438, 135604.
[39] Cheng, A. H. D. (2016). Poroelasticity (Theory and Applications of Transport in Porous Media, Vol. 27). Switzerland: Springer International Publishing.
[40] Liu, J., Chen, Z., Elsworth, D., Miao, X., & Mao, X. (2011). Evolution of coal permeability from stress-controlled to displacement-controlled swelling conditions. Fuel, 90(10), 2987-2997.
[41] Huang, Y., Shi, Z., Flottmann, T., Kuznetsov, D., Rudolph, V., Leonardi, C., & Chen, Z. (2021). Experimental study of coal directional sorption-induced strain under different temperatures. In Asia Pacific Unconventional Resources Technology Conference. Unconventional Resources Technology Conference.
[42] Zhang, H., Liu, J., & Elsworth, D. (2008). How sorption-induced matrix deformation affects gas flow in coal seams: a new FE model. International Journal of Rock Mechanics and Mining Sciences, 45(8), 1226-1236.
[43] Scherer, G. W. (1986). Dilatation of porous glass. Journal of the American Ceramic Society, 69(6), 473-480.
[44] Peng, Y., Liu, J., Pan, Z., Connell, L. D., Chen, Z., & Qu, H. (2017). Impact of coal matrix strains on the evolution of permeability. Fuel, 189, 270-283.
[45] Liu, J., Chen, Z., Elsworth, D., Miao, X., & Mao, X. (2010). Evaluation of stress-controlled coal swelling processes. International journal of coal geology, 83(4), 446-455.
[46] Zhou, H. W., Zhang, L., Wang, X. Y., Rong, T. L., & Wang, L. J. (2020). Effects of matrix-fracture interaction and creep deformation on permeability evolution of deep coal. International Journal of Rock Mechanics and Mining Sciences, 127, 104236.
[47] Day, S., Fry, R., & Sakurovs, R. (2008). Swelling of Australian coals in supercritical CO_2. International Journal of Coal Geology, 74(1), 41-52.
[48] Pan, J., Meng, Z., Hou, Q., Ju, Y., & Cao, Y. (2013). Coal strength and Young's modulus related to coal rank, compressional velocity and maceral composition. Journal of Structural Geology, 54, 129-135.
[49] Vishal, V., Ranjith, P. G., Pradhan, S. P., & Singh, T. N. (2013). Permeability of sub-critical carbon dioxide in naturally fractured Indian bituminous coal at a range of down-hole stress conditions. Engineering Geology, 167, 148-156.
[50] Tan, Y., Pan, Z., Liu, J., Zhou, F., Connell, L. D., Sun, W., & Haque, A. (2018). Experimental study of impact of anisotropy and heterogeneity on gas flow in coal. Part II: Permeability. Fuel, 230, 397-409.
[51] Tan, Y., Pan, Z., Liu, J., Kang, J., Zhou, F., Connell, L. D., & Yang, Y. (2018). Experimental study of impact of anisotropy and heterogeneity on gas flow in coal. Part I: Diffusion and adsorption. Fuel, 232, 444-453.
[52] Jia, Z., Li, C., Zhang, R., Wang, M., Gao, M., Zhang, Z., Ren, L., & Xie, J. (2019). Energy evolution of coal at different depths under unloading conditions. Rock Mechanics and Rock Engineering, 52(11), 4637-4649.

[53] Wei, M., Liu, J., Elsworth, D., Liu, Y., Zeng, J., & He, Z. (2021). Impact of equilibration time lag between matrix and fractures on the evolution of coal permeability. Fuel, 290, 120029.
[54] Apriyani, N., Momen, M., Djaelani, S., Sodli, A., Satria, A., & Murtani, A. S. (2014). Integrated cleat analysis and coal quality on CBM exploration in Sangatta II Field, Kutai Basin, East Kalimantan.
[55] Zeng, J., Liu, J., Li, W., & Guo, J. (2021). A process-based coal swelling model: Bridging the gaps between localized swelling and bulk swelling. Fuel, 293, 120360.
[56] Mostaghimi, P., Armstrong, R. T., Gerami, A., Hu, Y., Jing, Y., Kamali, F., Liu, M., Liu, Z., Lu, X., Ramandi, H. L., Zamani, A., & Zhang, Y. (2017). Cleat-scale characterisation of coal: An overview. Journal of Natural Gas Science and Engineering, 39, 143-160.
[57] Karacan, C. Ö. (2008). Evaluation of the relative importance of coalbed reservoir parameters for prediction of methane inflow rates during mining of longwall development entries. Computers & Geosciences, 34(9), 1093-1114.
[58] Wang, Z., Pan, J., Hou, Q., Niu, Q., Tian, J., Wang, H., & Fu, X. (2018). Changes in the anisotropic permeability of low-rank coal under varying effective stress in Fukang mining area, China. Fuel, 234, 1481-1497.
[59] Liu, Z., Liu, D., Cai, Y., & Pan, Z. (2020). Experimental study of the effective stress coefficient for coal anisotropic permeability. Energy & Fuels, 34(5), 5856-5867.
[60] Cui, X., Bustin, R. M., & Chikatamarla, L. (2007). Adsorption-induced coal swelling and stress: Implications for methane production and acid gas sequestration into coal seams. Journal of Geophysical Research: Solid Earth, 112(B10), B10202.
[61] Cao, P., Liu, J., & Leong, Y. K. (2016). A fully coupled multiscale shale deformation-gas transport model for the evaluation of shale gas extraction. Fuel, 178, 103-117.
[62] Tian, J., Liu, J., Elsworth, D., Leong, Y. K., & Li, W. (2023). An effective stress-dependent dual-fractal permeability model for coal considering multiple flow mechanisms. Fuel, 334, 126800.
[63] Wei, M. Y., Liu, J., Liu, Y. K., Liu, Z. H., & Elsworth, D. (2021). Effect of adsorption-induced matrix swelling on coal permeability evolution of micro-fracture with the real geometry. Petroleum Science, 18(4), 1143-1152.
[64] Tian, J., Liu, J., Elsworth, D., Leong, Y. K., & Li, W. (2022). Linking fractal theory to a fully coupled coal deformation and two-phase flow multiphysics: The role of fractal dimensions. Energy & Fuels, 36(20), 12591-12605.
[65] Li, W., Liu, J., Zeng, J., Leong, Y. K., Elsworth, D., Tian, J., & Li, L. (2020). A fully coupled multidomain and multiphysics model for evaluation of shale gas extraction. Fuel, 278, 118214.
[66] Harpalani, S., & Chen, G. (1995). Estimation of changes in fracture porosity of coal with gas emission. Fuel, 74(10), 1491-1498.
[67] Zhi, S., Elsworth, D., & Liu, L. (2019). W-shaped permeability evolution of coal with supercritical CO_2 phase transition. International Journal of Coal Geology, 211, 103221.
[68] Zeng, J., Liu, J., Li, W., Leong, Y. K., Elsworth, D., & Guo, J. (2021). Shale gas reservoir modeling and production evaluation considering complex gas transport mechanisms and dispersed distribution of kerogen. Petroleum Science, 18(1), 195-218.
[69] Tang, S., Wan, Y., Duan, L., Xia, Z., & Zhang, S. (2015). Methane adsorption-induced coal swelling measured with an optical method. International Journal of Mining Science and Technology, 25(6), 949-953.
[70] Zhang, R., & Liu, S. (2017). Experimental and theoretical characterization of methane and CO_2 sorption hysteresis in coals based on Langmuir desorption. International Journal of Coal Geology, 171, 49-60.

[71] Pan, R., Cheng, Y., Yuan, L., Yu, M., & Dong, J. (2014). Effect of bedding structural diversity of coal on permeability evolution and gas disasters control with coal mining. Natural Hazards, 73(2), 531-546.
[72] Lau, H. C., Li, H., & Huang, S. (2017). Challenges and opportunities of coalbed methane development in China. Energy & Fuels, 31(5), 4588-4602.
[73] Robertson, E. P., & Christiansen, R. L. (2007). Modeling laboratory permeability in coal using sorption-induced-strain data. SPE Reservoir Evaluation & Engineering, 10(03), 260-269.
[74] Wang, S., Elsworth, D., & Liu, J. (2011). Permeability evolution in fractured coal: the roles of fracture geometry and water-content. International Journal of Coal Geology, 87(1), 13-25.
[75] Connell, L. D., Pan, Z., Lu, M., Heryanto, D., & Camilleri, M. (2010). Coal permeability and its behaviour with gas desorption, pressure and stress. In SPE Asia Pacific Oil and Gas Conference and Exhibition. Society of Petroleum Engineers.
[76] Wang, Y., Liu, S., & Zhao, Y. (2018). Modeling of permeability for ultra-tight coal and shale matrix: A multi-mechanistic flow approach. Fuel, 232, 60-70.
[77] Roy, S., Raju, R., Chuang, H. F., Cruden, B. A., & Meyyappan, M. (2003). Modeling gas flow through microchannels and nanopores. Journal of Applied Physics, 93(8), 4870-4879.
[78] Jaeger, J. C., Cook, N. G., & Zimmerman, R. (2009). Fundamentals of Rock Mechanics. John Wiley & Sons.
[79] Amadei, B. (2012). Rock Anisotropy and the Theory of Stress Measurements (Vol. 2). Springer Science & Business Media

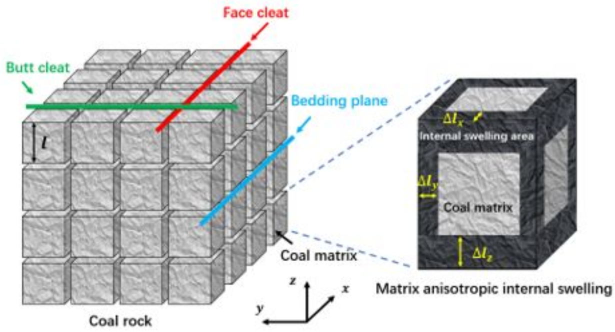

For Table of Contents Only